Obtaining Directionality from Scattering and Capture in Fast Neutron Detectors

by

Tingshiuan C. Wu

A dissertation submitted in partial fulfillment
of the requirements for the degree of
Doctor of Philosophy
(Nuclear Engineering and Radiological Sciences)
in The University of Michigan
2023

Doctoral Committee:

Professor Igor Jovanovic, Chair
Doctor Steven A. Dazeley, Lawrence Livermore National Laboratory
Doctor Mark Hammig
Professor Al Hero
Professor Sara Pozzi

Tingshiuan C. Wu
wutingsh@umich.edu
ORCID ID: 0000-0003-3373-2163

ACKNOWLEDGEMENTS

I would like to first thank my advisor, Professor Igor Jovanovic, who has helped guide and support me though my studies. You have provided me with encouragement, opportunities, and lessons throughout this experience that has helped me develop as a scientist and that will certainly be beneficial for my future endeavors. I would also like to thank Steven Dazeley for additional insight and advice for my dissertation work. I would also like to thank the members of my dissertation committee – Professor Sara Pozzi, Doctor Steve Hammig, and Professor Al Hero for their insights and recommendations through out the dissertation process.

In addition, I would like to thank the members of the SANDD/iSANDD group Viacheslav A. Li, Felecia Sutanto, and Timothy Classen for their feedback and insights gained from their parallel work. I would also like to thank the other members of the Applied Nuclear Science Group: Tan Shi for helping me develop ideas for the composite shards detector work, Kris Ogren, Felicia Sutanto, and Jason Natress for their insight and assistance in helping me develop skills in data analysis in ROOT and development of simulations in Geant4, as well as Oskar Searfus and Colton Graham, and Andrew Wilhelm for their feedback and insight. I would also like to thank my colleagues in other groups in the Nuclear Engineering department, particularly Stefano Marin, Christopher Meert, Matthew Petryk, Abbas Jinia, and many others for their friendship and support throughout my graduate studies. I would also like to thank our graduate coordinator Garnette Roberts for his help in navigating the requirements for my graduate degree. I would also like to thank the engineers at PETsys electronics

for their insight, patience, and assistance with the Time of Flight Positron Emission Tomography 2 (TOFPET2) ASIC; this work would not have been possible without their advice.

I would also like to thank Professor Tatjana Jevremovic and Professor Dave Kieda for mentoring my research at the University of Utah, which helped me lay the foundation for my scientific career. I would also like to thank Doctor Jason Burke at Lawrence Livermore National Laboratory for introducing me to the field of nuclear detection and providing me a wonderful experience at a national laboratory.

I also thank my parents Mingin Wu and Sueh-Lin Cheng as well as my sister Tingyee R. Wu for their encouragement and support throughout the highs and lows of my graduate years.

Finally, I would like to acknowledge the organizations and funding sources that made my research possible. This research was supported by the Department of Energy Nuclear Energy University Program Fellowship, the Department of Energy National Nuclear Security Administration Consortium for Monitoring, Verification and Technology (DE-NE000863), and the US Department of Homeland Security [2015-DN-077-ARI096].

TABLE OF CONTENTS

LIST OF FIGURES

Figure

LIST OF TABLES

Table

LIST OF ABBREVIATIONS

ADC analog to digital converter unit

ASIC application-specific integrated circuit

DAQ data acquisition

DD deuterium-deuterium

DT deuterium-tritium

FEB front end board

FEM front end module

FOM figure of merit

FWHM full-width half-maximum

LED light emitting diode

NPT Treaty on the Non-Proliferation of Nuclear Weapons

PET positron emission tomography

PMT photomultiplier tube

PSD pulse shape discrimination

PSP pulse shape parameter

PVT polyvinyl toluene

QDC charge to digital converter

SANDD Segmented AntiNeutrino Directional Detector

SiPM silicon photomultiplier

TDC time to digital converter

TOFPET2 Time of Flight Positron Emission Tomography 2

ABSTRACT

Neutron detection with directional sensitivity is an increasingly sought-after technology in nuclear safety and security. To keep the nuclear material secure, an accurate assessment of its material composition, quantity, and location is needed. The location of a source can be narrowed down with directional detection. Detection of neutrons is needed for this application due to the increased difficulty for an adversary to shield neutrons to evade detection as opposed to γ radiation. Directional detection requires position sensitivity in the detector volume to obtain information from which directionality can be reconstructed. One approach to achieve position-sensitive neutron detection is the use of recoil-capture composite scintillators comprising of a neutron recoil and neutron capture component coupled with an array of silicon photomultiplier (SiPM) pixels. This dissertation encompasses work to advance the development of directional recoil-capture neutron scatter cameras, which share much of the underlying technology with highly segmented reactor antineutrino detectors.

To discriminate neutrons from γ radiation, differences in pulse shapes are exploited in a process known as pulse shape discrimination (PSD). Detector designs that contain a capture element such as ^{6}Li can also uniquely identify neutron captures. The first section of this dissertation extends previous work on heterogeneous composite detectors that comprise a polyvinyl toluene (PVT) recoil component and a ^{6}Li glass capture component. In such detectors, it is found that charged particles depositing energy through two different materials can produce composite pulse shapes with pulse shape characteristics dependent on the proportion of energy deposited in each material. The nature of composite pulse shapes in such heterogeneous detectors is investigated

through experimentation with a representative composite detector with 500-µm shards and 7 wt.% ^{6}Li glass loading. This detector is also simulated in Monte Carlo simulation to find energy deposition fractions in the two materials. An estimate for the resulting PSP is made by combining PVT and ^{6}Li glass waveforms from averaged experimental waveforms and the simulated energy deposition fraction. From this, a 3σ-region γ rejection was reconstructed for the 7 wt.%. In addition, estimates for other ^{6}Li glass loadings were obtained. Some discrepancies are identified between the simulation and experiment, and the simulation of the effect of uneven shard distribution suggests a possible explanation.

To gain insight into the potential contribution of capture location information can have on improving directionality information, a Bayesian updating approach is applied to an idealized spherical detector 12.7 cm in diameter. Lookup tables describing the likelihood of the interaction types and locations were constructed with Geant4 simulations of 10^6 incident neutrons per angle. Using these lookup tables, Bayesian updating was performed on a sequence of simulated events with an identical setup but a different random number seed to find the improvement of the angular estimate with each additional incident neutron. The recoil-only case was compared to the case with recoil with capture. When a low light output threshold is set, there is no significant improvement in the angular estimate after a given number of trials. However, in cases where the neutron/γ discrimination threshold is high, neutron capture was able to improve an angular estimate of incoming neutron direction by $\sim 20^\circ$ for 100 incident neutrons due to the recovered recoil events that would fall below the discrimination threshold.

In practice, position information is not exactly known and thus arrays with tens to hundreds of channels are needed to attain acceptable event position resolution. The feasibility of using an application-specific integrated circuit (ASIC) was investigated for data acquisition, as ASICs provide high channel densities at low cost-per-channel.

However, the lack of waveform digitization in many of these systems precludes the use of full waveform analysis for PSD. In this work, an ASIC designed for positron emission tomography (PET) imaging, Time of Flight Positron Emission Tomography 2 (TOFPET2), was adapted for use in pulse-sensitive measurement. Pulse shape sensitivity was obtained by splitting an input signal from a SiPM into two channels to be integrated over two different periods. Rudimentary PSD was shown for a stilbene cube exposed to a ^{252}Cf source mounted on a SiPM, with a PSD figure of merit (FOM) of 1.190. In addition, an light emitting diode (LED)-based calibration system was developed to correct for nonlinearities in the SiPM/ASIC system. To obtain the calibration curve, an LED powered by a square pulser with varying pulse lengths and amplitudes produced light pulses and was measured by the SiPM/ASIC system. The light was also measured using a photodiode with a full waveform digitization readout. A dependence of the calibration curve on pulse shape was observed at more intense light levels. With this limitation, an operational range was established where the calibration curve is independent of pulse shape, and spectroscopy using stilbene attached to a SiPM was performed with three γ sources, a DD neutron generator source and a ^{252}Cf mixed neutron/γ source.

CHAPTER 1

Introduction

1.1 Nuclear Nonproliferation

On the 8th of August, 1945, the destructive potential of atomic nuclei was revealed to the world with the atomic bombing of Hiroshima. However, nuclear technology has subsequently come to be used for peaceful purposes, notably the production of clean energy and the application of nuclear technology in medicine. Although nuclear power had improved the lives of many, the continual buildup of nuclear arms throughout the course of the Cold War raised concerns about the danger that the proliferation of nuclear weapons technology can pose. Several more countries developed and tested nuclear weapons early: the Soviet Union in 1949, the United Kingdom in 1952, France in 1960, and China in 1964. The Treaty on the Non-Proliferation of Nuclear Weapons (NPT) [3] was pivotal as it established an agreement that would ensure that humanity could continue to use nuclear technology peacefully while mitigating its risks. Under the treaty, further proliferation of nuclear technology would be limited to the five states which possessed them at the time and the existing nuclear weapons states would work toward disarmament. In the years since there still are challenges to non-proliferation: India, Pakistan, Israel, and DPR Korea, all of which are non-signatories of the NPT (DPR Korea was a signatory but has since withdrawn) have developed their own nuclear weapons programs. Enforcement of this treaty and

subsequent nonproliferation treaties requires the accounting of nuclear material to prevent malicious actors from developing nuclear weapons. The ratification of the NPT and subsequent treaties, and the work of international agencies such as the International Atomic Energy Agency, have enabled peaceful uses of nuclear science and technology such as the production of clean energy and medical diagnostics and treatment.

In order to achieve the nonproliferation goals, it is necessary to control the production and transport of material that may be used to develop nuclear weapons and to prevent the trade of such material. The United States has deemed these materials "special nuclear material", defined in the Atomic Energy Act of 1954 [4]. These materials include plutonium and uranium enriched in ^{233}U or ^{235}U [4]. In addition, the development of fourth-generation and small modular reactors will lead to the increased complexity of fuel cycles, which can complicate nuclear material accounting.

To keep nuclear material secure, an accurate assessment of its material composition, quantity, and location is needed. To detect special nuclear material, γ radiation and neutrons are of particular interest as they are able to penetrate relatively thick objects. To detect the presence of such material, a detector could observe the radiation from a potential source passively, known as passive interrogation, or the potential source could be interrogated with γ or neutron radiation, known as active interrogation [5]. Though γ-ray signatures alone can be effective at identifying such material, detection may be defeated by using a sufficiently thick layer of high-Z materials such as lead. For cases such as these, fast neutron detection is necessary due to the increased difficulty of shielding them. An ability to measure the fast neutron energy spectrum can allow for the discrimination between different source types, such as highly enriched uranium (HEU) and natural uranium.

Passive interrogation involves the detection of the emission of fast neutrons and γ radiation. Passive interrogation is primarily of practical interest for the detection of

plutonium, as the low yield of ^{235}U spontaneous fission makes passive measurements of such neutrons impractical, for which active interrogation where fission would be induced would be more desirable[6]. In passive interrogation systems, fast neutrons produced from spontaneous fission and their multiplied neutrons are detected and discriminated from the background and γ radiation through the use of a detector capable of particle discrimination.

1.2 Neutron Detection

Neutrons may be detected via their scattering or capture within the detector volume. In an elastic scattering (n, n) interaction, the neutron scatters off a nucleus within the detector volume. In a scintillation detector, these recoiled nuclei induce light emission which can be detected by a light detector such as a photomultiplier tube (PMT) or a silicon photomultiplier (SiPM). In this process, a portion of the neutron's kinetic energy E_{n} is imparted on the target nucleus ^{A}X with the atomic mass number A, yielding a well-known relationship derived from the conservation of energy and momentum:

$$E_{^{A}\mathrm{X}} \approx \frac{4A}{(1+A)^2}\left(\cos^2\theta\right) E_{\mathrm{n}}. \tag{1.1}$$

The maximum energy is imparted to the nucleus in a head-on elastic scatter where $\theta = 0$:

$$E_{^{A}\mathrm{X}}\Big|_{\mathrm{max}} \approx \frac{4A}{(1+A)^2} E_{\mathrm{n}}. \tag{1.2}$$

The energy transferred to ^{A}X, and thus the detectable energy, is maximized for low values of A. It is thus ideal for scintillation detectors used for detecting neutrons to consist of material with low A, such as ^{1}H, whose nucleus is simply a proton. In this

case, the energy imparted to the proton E_{p} is simply:

$$E_{\mathrm{p}} \approx E_{\mathrm{n}} \cos^2 \theta \tag{1.3}$$

$$E_{\mathrm{p}} \Big|_{\mathrm{max}} \approx E_{\mathrm{n}}. \tag{1.4}$$

For scintillation detectors, organic scintillators are favored due to their high number density of protons for neutrons to recoil from. Though most detector systems use proton recoil to detect fast neutrons, other small nuclei are also used for their unique advantages, such as ^{2}H [7] and ^{4}He [8, 9].

Alternately, neutron capture (n, γ) may be employed. In these detectors, an incident neutron is captured by a material $^{A}\mathrm{X}$ to form $^{A+1}\mathrm{X}$:

$$\mathrm{n} + {}^{A}\mathrm{X} \longrightarrow {}^{A+1}\mathrm{X}. \tag{1.5}$$

The resulting mass difference is reflected in the Q value of the reaction, which is detected:

$$Q = c^2 \left(m_{A+1\mathrm{X}} - m_{A\mathrm{X}} - m_{\mathrm{n}} \right). \tag{1.6}$$

For these detectors, a material with a high neutron capture cross-section such as ^{6}Li or ^{10}B [10] is used as the capture agent. Since the interaction cross-section for neutron capture is highest at low neutron energies, the neutron is typically first thermalized in hydrogen-rich material, which can be nearby or within the detector itself [11]. A rough diagram of this process is shown in Fig. 1.1. The energy deposited in the material is nearly equal to the Q value of the reaction type, independent of the incoming kinetic energy of the neutron prior to thermalization. The energy of the incoming neutron may still be inferred if the thermalization recoils are detected through capture-gated spectroscopy [12]. In addition, some capture reactions have been shown have a response

dependent on incoming neutron energy, notably Cs_2LiYCl_6:Ce (CLYC), for which the $^{35}Cl(n,p)^{35}S$ deposits a proton with energy that varies linearly with the incoming neutron[13, 14].

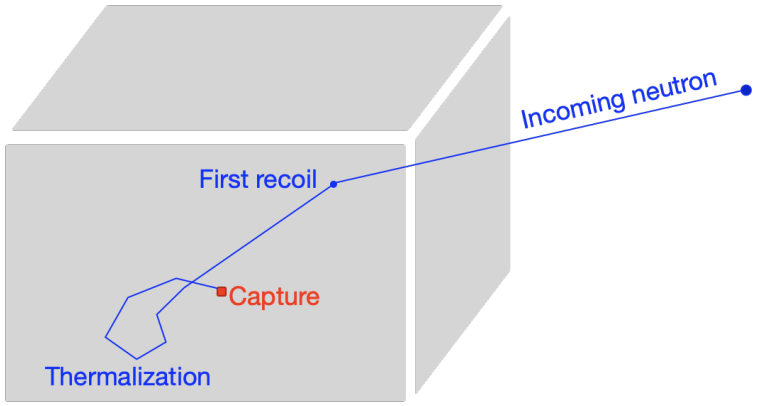

Figure 1.1: Diagram of the thermalization and capture process in a detector that is capable of neutron capture

1.3 Pulse shape discrimination (PSD) in scintillators

Many organic scintillation detectors are sensitive to both neutron radiation and γ radiation. For useful spectroscopy, then, it is necessary to discriminate between events of different types from different particles, *e.g.*, Compton scattering of γ rays and proton recoils induced by fast neutrons. One way of discriminating between these events is through pulse shape discrimination (PSD). PSD exploits differences in the time profiles of the pulses produced by radiation of different types in some detector materials.

In organic scintillators, this is possible due to the different ratios of short-lived singlet states and long-lived triplet states for electrons versus heavy charged particles such as protons[10, 15, 16]. These singlet and triplet states are present in the molecular structure of certain organic molecules such as stilbene; excitation and subsequent de-excitation of these states are responsible for the production of scintillation light [15]. The long-lived triplet states emit scintillation light through the collision triplet states

into singlet states (thus the resulting scintillation light is emitted with the same wavelength but at a different timescale). As this process is dependent on bimolecular interactions, the triplet state collision process is more abundant in short ionization tracks with high excitation densities, such as those by protons or other heavy charged particles [16, 17].

Alternatively, differing pulse shapes can also be the result of the interaction radiation with different materials in composite scintillators [2, 11, 18]. A case where two different materials yield a "composite" pulse shape is studied extensively in Ch. 2 of this dissertation, and this composite material consists of a heterogeneous assembly of an organic polyvinyl toluene (PVT) element and a neutron-capturing glass scintillator. The glass is doped with an isotope that has a high neutron capture cross-section such as ^{6}Li or ^{10}B. The scintillating glass material used in this dissertation, GS-20, contains ^{6}Li and is doped with Ce^{3+} activators to produce the scintillation light [10, 19–21].

In a common implementation of PSD, a raw waveform is taken, and two integrals are calculated of the resulting baseline-subtracted waveform: the tail integral and the total integral, as shown in Fig.1.2. The ratio between the tail and total integrals is frequently defined as the pulse shape parameter PSP used to discriminate between neutron and γ radiation:

$$PSP \equiv \frac{Q_{\text{tail}}}{Q_{\text{total}}} \tag{1.7}$$

1.4 Fast neutron directionality with silicon photomultiplier-based detector arrays

In various nuclear safeguards scenarios, it is desirable to detect the directionality of incoming fast neutrons. For instance, a proximity search of a large number of

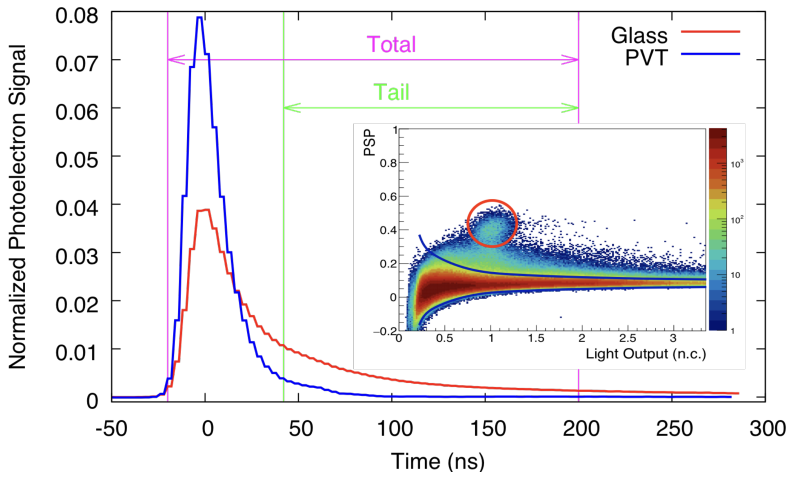

Figure 1.2: Averaged pulse shape and PSD diagram for a composite PVT and ^{6}Li doped glass shards detector. The PSD in this type of detector is discussed in length in Ch. 2.

containers for special nuclear material at a port would be prohibitively time-consuming. Fast neutron directionality may be employed as an alternative to infer the location of incoming sources. Information on a neutron source's position would allow for an enhancement of the signal-to-background ratio or at least narrow down a proximity search. There are various ways to obtain fast neutron directionality: the coded aperture which involves an array of detectors behind a "mask" with a known pattern [22], the time projection chamber which uses a pressurized volume gas along with an electric and magnetic field to reconstruct the position and momentum of recoiling particles [23, 24], and the neutron scatter camera, where two neutron events such as neutron scatters are detected with position sensitivity to reconstruct the incoming neutron angle [25–27]. In a double scatter camera, the positions of two neutron scatters to reconstruct a cone of possible incoming neutron angles [25]. In general, a neutron scatter camera employs an array of several detector segments which are read out separately [27]. Information about an incoming neutron can be thus inferred from the signals recorded in various detector segments with which the neutron has interacted. For example, in a neutron double-scatter camera a fast neutron is detected

twice via proton recoil in two different detector segments in order to reconstruct a cone of possible incoming neutron angles [26]. Of particular interest to this work is the so-called single-volume scatter camera [26, 27]. In one form of the single-volume scatter camera, the detector volume is segmented into several parts, and read out using a multi-pixel light detector. These light detectors may include an array of photomultiplier tubes or a silicon photomultiplier (SiPM) array.

A SiPM pixel consists of hundreds of single-photon avalanche photodiodes (SPADs) in Geiger mode [10, 28]. Each subpixel is sensitive to single photons, and the light output of the scintillator can be measured by summing the number of triggered subpixels. Silicon photomultipliers have the advantage over photomultiplier tubes in that they do not necessitate high voltage supplies and can operate at voltages on the order of tens of volts.

This dissertation expands upon the prior development and characterization of the Segmented AntiNeutrino Directional Detector (SANDD) detector [29, 30], which was developed for antineutrino detection rather than the detection of fast neutrons. The SANDD detector is a detector array of 64 lithium-doped plastic scintillator rods mounted on a SiPM array. This detector is read out from two SiPMs on both sides of each rod, with position resolution in the x and y directions obtained through the identification of the triggered SiPM pixel, and the z direction inferred through the time difference or the relative amplitude of signals detected on the two sides of the rod. One way in which this dissertation expands upon the SANDD detector is an investigation into compact data acquisition (DAQ) readouts in Ch. 4 and 5. Whereas the DAQ of SANDD consists of an entire cabinet of full-waveform digitization modules, the use of an application-specific integrated circuit (ASIC) for DAQ would miniaturize the DAQ setup, allowing it to be used for other applications such as nuclear safeguards.

1.5 ASIC-based readouts for SiPM arrays and Time of Flight Positron Emission Tomography 2 (TOFPET2)

In segmented detector arrays such as those used in neutron scatter cameras, the position resolution of neutron interactions requires a finer segmentation with more detector channels as a finer segmentation would improve interaction position resolution. The multitude of channels in these detector arrays poses a practical challenge in that reading out large numbers of channels can be resource-intensive in cost, physical footprint, and power consumption. As an example, the SANDD antineutrino detection array using two sets of SiPMS with 64 pixels each would take 128 channels, which could take a large cabinet of electronics. Although this does not necessarily pose a problem in a typical antineutrino detection setup, the large physical footprint would impact the practicality of use in a safeguards setting.

Miniaturization of the data acquisition (DAQ) can be achieved using purpose-built ASICs. The use of ASICs allows data acquisition circuits to be fabricated directly on hardware in a manner optimized for a particular purpose, which reduces the footprint significantly at the cost of flexibility. One such ASIC is the TOFPET2 [31], standing for "time of flight positron emission tomography". A typical application of this DAQ in positron emission tomography (PET) systems involves the use of two LYSO scintillators to detect two electron-positron annihilation photons at 511 keV. Although the application of this ASIC is not directly related to neutron scatter camera detector arrays, this PET DAQ already exists commercially and has features that can be potentially used for PSD, notably the ability to modify charge integration time on a per-channel basis. Although the intended application of the TOFPET2 system is quite different, this investigation may motivate further development of such electronics in the future.

1.6 Dissertation Structure

The following chapters contain standalone contributions to the development of directional fast neutron detection for scintillation detectors comprising both a recoil and capture component. Composite scintillators are studied in Ch. 2, with the investigation of compound pulse shapes for a heterogeneous recoil-capture detector, a design with ^{6}Li shards suspended in a PVT matrix, and how the heterogeneity affects γ rejection via PSD. For the development of directionality for recoil-capture scatter arrays, Ch. 3 covers the development of angular reconstruction using recoil and capture using a Bayesian method on a Monte Carlo simulation. Ch. 4 covers work on adapting an ASIC-based readout designed for positron emission tomography, TOFPET2, for a neutron scatter camera with PSD capabilities. Finally, Ch. 5 covers work characterizing a light emitting diode (LED)-based calibration method for a SiPM-mounted to the TOFPET2.

CHAPTER 2

PSD in Composite Scatter-Capture Scintillators

The content of this chapter has been adapted from Ref. [2].

2.1 Introduction

Heterogeneous composite scintillators utilize fast neutron thermalization and capture for neutron detection and are a promising technology for fast neutron detection in intense γ-ray fields such as those found in active interrogation environments [1, 11, 32–38]. These can additionally utilize PSD to distinguish neutron thermalization from γ- ray interactions [39]. One such composite scintillator type uses a scintillating PVT matrix with ^{6}Li glass embedded into the detector volume [11, 32, 35]. In that design, fast neutrons can be detected via elastic scattering in the PVT followed by neutron capture in GS20 Ce^{3+}-doped ^{6}Li scintillating glass [1, 20]. The EJ-290 PVT used has a decay time of $\sim 3\,\text{ns}$, an index of refraction of 1.58, and a light output of $10\,000\,\text{photons} \cdot \text{MeV}^{-1}$ (58 % of anthracene)[40]. The GS20 scintillating glass has a decay time of 57 ns, an index of refraction of 1.55, and a light output of $4350\,\text{photons} \cdot \text{MeV}^{-1}$ (25 % of anthracene) [41]. This type of detector combines desirable and complementary features of the two materials: the high hydrogen density of PVT as a moderator and the high neutron capture cross-section and Q-value of the capture reaction on ^{6}Li. In addition, the detection of proton recoil in the PVT

allows for neutron spectroscopy via capture gating [12, 42, 43]. Scintillation from the PVT and ^{6}Li glass can be distinguished from each other via PSD; this aids the identification of neutron capture events. To quantify the PSD, the tail integral/total integral ratio is frequently used and is defined as the pulse shape parameter (PSP). The fluorescence lifetime of glass is considerably longer than that of the PVT and the neutron capture in glass produces a consistent light output associated with the capture Q-value ($Q = 4.78\,\text{MeV}$). Thus, when such a PVT/^{6}Li glass composite detector is exposed to a mixed neutron/γ radiation field, a neutron capture "island" (*i.e.* a small region in PSP-light output parameter space) is observed, as shown in Fig. 2.1. Lithium glass is also sensitive to γ radiation but like PVT, it cannot discriminate neutron from γ events. However, electrons produced in the glass are also likely to interact with the PVT since their range is considerably longer than the size of the glass particles and the mean distance between glass particles, and this produces a compound pulse shape. This type of detector has been constructed [1, 11, 39] and successfully used in nuclear security applications for low-energy neutron detection, including detecting delayed neutrons in active interrogation [44], discriminating uranium isotopes using the time emission profiles of long-lived delayed neutrons [45], and disambiguating delayed neutrons from different generations of fission [46].

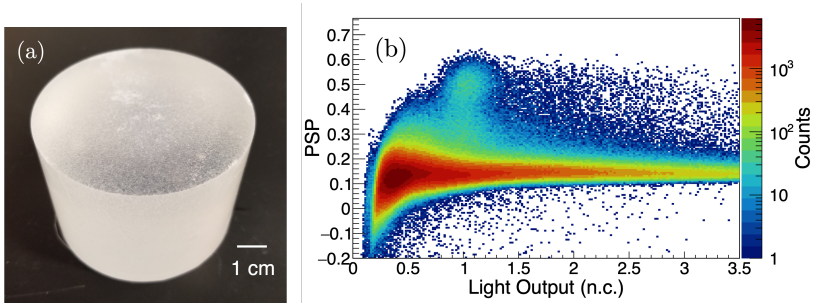

Figure 2.1: (a) PVT-glass shards detector used in this study [1]; (b) detector response when exposed to a ^{252}Cf source. The light output is normalized to neutron capture (n.c.) units, where the value of unity represents the detected light output due to low-energy neutron capture in ^{6}Li glass. *Figure adapted from Ref. [2].*

In previous studies, ^{6}Li glass in the form of thin, long rods was used to construct a

composite detector [11]. However, the fabrication process for this particular geometry suffers from high cost, which is dominated by the limited commercial availability of rods. Therefore, shards-geometry detectors, which can be less costly to fabricate, are being investigated as an alternative [33]. In the shards-geometry configuration, the ^{6}Li glass is randomly and uniformly distributed in the PVT as discussed in Ref. [47]. To fabricate this type of detector, ^{6}Li glass is crushed using a vibrational ball mill and added to the PVT using a vibrational mixer [1, 47]. The principal design aspects of such a detector include shard size and shard loading, defined as the weight percent of ^{6}Li glass in the composite scintillator. Increasing the shard loading improves the neutron detection efficiency at the cost of poorer γ rejection. Here, γ rejection is defined by the fraction of incident γ rays from a ^{60}Co sourcemisidentified as neutrons. For this work, an identification region of 3σ in the light-PSP space is used as this definition of γ rejection has been used in prior work with similar scintillator detectors [1, 11, 33, 45, 47]. The main subject of this study is the effect of ^{6}Li glass loading levels on the γ rejection performance in the glass shard geometry, but the developed methodology is generally applicable to heterogeneous scintillators for various geometries and constituent materials. For this work, a composite detector with 500 µm average diameter glass shards and 7 wt.% ^{6}Li glass loading is used. The average shard size distribution was measured using a scanning electron microscope [47]. The distribution of shard sizes averaging 500 µm was obtained from the authors of Ref. [47], and the shards were simulated as spheres based on this distribution.

The limited γ rejection in these composite scintillators can be attributed to the fact that energy deposition from γ radiation may occur in the glass as well as in the PVT, regardless of where the initial interaction takes place. This is because the energetic electron produced in a γ interaction can have a long enough range to pass through both the glass and the PVT, causing both materials to simultaneously emit fluorescence. This effect is likely in a shards-geometry configuration with high

glass loading due to the increased likelihood of an electron track passing through glass. The resulting scintillation time characteristic can be considered a "composite pulse", with light output contributions from both the relatively slowly decaying glass fluorescence and the more rapidly decaying PVT fluorescence. The decay observed from such a scintillator and the associated PSP lie somewhere between the PSP for the glass-only energy deposition and the PVT-only energy deposition. This tendency has a detrimental effect on the γ rejection: the PSP and light output resulting from partial energy deposition in glass may fall within the neutron capture region. For example, the rods-geometry detector discussed in Ref. [11] has a 3σ γ rejection of $<10^{-6}$, while the γ rejection of this shards detector is $\sim 10^{-4}$ [1].

As a result, a trade-off exists when increasing the ^{6}Li glass loading: the neutron detection efficiency improves at the expense of γ rejection performance. To quantify this trade-off it is desirable to develop a model to predict the γ rejection for different shard sizes and loadings. In this work, a model is developed to construct the waveforms that result from energy deposition in multiple materials. The input to the model is the energy deposition simulated in the Monte Carlo code Geant4 [48]. By using this model in conjunction with Geant4 simulations, the γ rejection characteristics of a detector with a particular geometry and shards configuration can be predicted, which informs the detector design.

2.2 Heterogeneous composite scintilator model

We model a heterogeneous scintillator composed of two material components, a ^{6}Li-containing scintillating glass and scintillating PVT, both of which by themselves do not exhibit PSD. In such a detector, we highlight four canonical types of energy deposition which may occur when the detector is exposed to γ or neutron radiation(Fig. 2.2):

A. Fast electrons produced in γ-ray induced interactions deposit their entire energy

within the PVT; this is the most common form of energy deposition for incident γ radiation when the glass loading is small.

B. Fast electrons deposit their energy in *both* the PVT and the glass, resulting in a scintillation time profile that is an intermediate between PVT and glass.

C. A neutron is captured on ^{6}Li in glass and produces heavy charged particles that deposit their entire energy within the glass.

D. A heavy charged particle (produced by neutron capture in glass or by neutron scattering in PVT, for instance) traverses both the glass and the PVT volume.

Although it is also possible for a recoil electron to deposit all of its energy in the glass, these events are highly unlikely for energetic electrons due to their range greatly exceeding the characteristic dimensions of a glass shard.

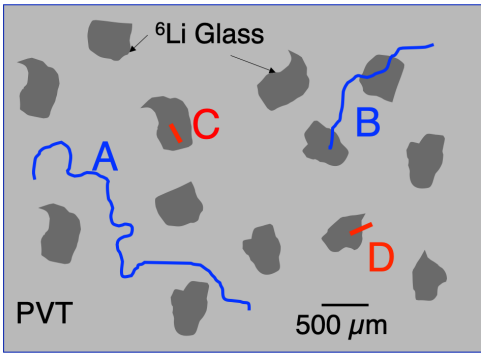

Figure 2.2: Illustration of several common electron and heavy charged particle event topologies in a heterogeneous composite scintillator. A: energetic electron deposits energy only in PVT; B: energetic electron deposits energy in both PVT and ^{6}Li glass; C: heavy charged particle from neutron capture deposits energy solely in ^{6}Li glass; D: heavy charged particle deposits energy in both ^{6}Li glass and PVT. The interaction type D is not discussed further in this work, since the γ rejection is of primary interest. *Figure adopted from [2].*

In our model, we denote the ^{6}Li glass and PVT components of the detector with superscripts "glass" and "PVT", respectively. The time-dependent detected light output from such scintillators for electrons, $\mathcal{L}_e(E_e, t)$, and heavy charged particles,

$\mathcal{L}_h(E_h, t)$, may be described as a sum of two contributions:

$$\mathcal{L}_e(E_e, t) = \mathcal{L}_e^{\text{glass}}(E_e^{\text{glass}}, t) + \mathcal{L}_e^{\text{PVT}}(E_e^{\text{PVT}}, t) \tag{2.1}$$

$$\mathcal{L}_h(E_h, t) = \mathcal{L}_h^{\text{glass}}(E_h^{\text{glass}}, t) + \mathcal{L}_h^{\text{PVT}}(E_h^{\text{PVT}}, t). \tag{2.2}$$

Here, E_e and E_h are the energies deposited by electrons (e) or heavy charged particles (h), respectively. This energy deposition is partitioned between the glass and PVT components of the scintillator:

$$E_e = E_e^{\text{glass}} + E_e^{\text{PVT}} \tag{2.3}$$

$$E_h = E_h^{\text{glass}} + E_h^{\text{PVT}}. \tag{2.4}$$

Each component material has a characteristic emission spectrum, and the emitted light from different materials may be attenuated by different amounts in transport to the light detector (such as a photomultiplier tube). To simplify the model, it is assumed that the light transport efficiency and the time profile of the detected light output are independent of the location of energy deposition. The light output due to electrons and heavy charged particle energy depositions is further separable in its energy (L) and time (S) dependence:

$$\mathcal{L}_e^{\text{glass}}(E_e^{\text{glass}}, t) = L_e^{\text{glass}}(E_e^{\text{glass}})S^{\text{glass}}(t) \tag{2.5}$$

$$\mathcal{L}_h^{\text{glass}}(E_h^{\text{glass}}, t) = L_h^{\text{glass}}(E_h^{\text{glass}})S^{\text{glass}}(t) \tag{2.6}$$

$$\mathcal{L}_e^{\text{PVT}}(E_e^{\text{PVT}}, t) = L_e^{\text{PVT}}(E_e^{\text{PVT}})S^{\text{PVT}}(t) \tag{2.7}$$

$$\mathcal{L}_h^{\text{PVT}}(E_h^{\text{PVT}}, t) = L_h^{\text{PVT}}(E_h^{\text{PVT}})S^{\text{PVT}}(t). \tag{2.8}$$

Here, it is assumed that neither the glass nor the PVT scintillator provide PSD and that the characteristic pulse shapes from those two materials are described by normalized shape functions $S^{\text{glass}}(t)$ and $S^{\text{PVT}}(t)$, respectively. The area under the

shape functions is normalized to unity. Neutron captures occurring in the glass with heavy charged particle energy deposition in glass are represented by Eq. (2.6), where the light output is a constant due to the relatively large Q-value compared to expected neutron energy at which the capture occurs. It is possible for one or both of the ^{6}Li capture reaction products to cross the glass/PVT boundary and deposit some of their energy in the PVT. However, this would not modify the γ rejection performance of the detector; instead, it would affect the neutron capture efficiency. Due to near-linearity of light output with deposited electron energy, one can write

$$L_e^{\text{glass}}(E_e^{\text{glass}}) = \kappa_e^{\text{glass}} E_e^{\text{glass}} \tag{2.9}$$

$$L_e^{\text{PVT}}(E_e^{\text{PVT}}) = \kappa_e^{\text{PVT}} E_e^{\text{PVT}}, \tag{2.10}$$

where κ is the proportionality constant for energy depositions by electrons, which also includes the effects of light transport efficiency and quantum efficiency of the photodetector. In contrast, the light output for heavy charged particles is nonlinear in energy; such a proportionality constant may not be used.

2.3 Experimental measurement of pulse shape and γ rejection

To obtain the characteristic pulse shapes needed for the model and to examine the validity of the model, experiments with a composite shards scintillator consisting of EJ-290 PVT and with 500-µm diameter GS20 glass shards ^{6}Li loaded at 7 wt.% (shown in Fig. 2.1) was performed. In this type of detector, a GS20 glass block is crushed and seived to a desired size, in this case 500 µm. Other shard sizes have been manufactured but have not been studied in this work. Fabrication of this scintillator is discussed in Ref. [1]. The scintillator is cylindrical and has a diameter of 76.2 mm and a height of 76.2 mm. The scintillator was mounted on a 2-inch diameter Hamamatsu R6231 photomultiplier tube using a light guide, and EJ-550 optical grease was applied

between the light guide and the PMT, as well as between the light guide and the scintillator. A reflective Teflon coating is applied on the scintillator, as well as a dark outer coating. A bias voltage of −1150 V was applied to the photomultiplier tube.

In the first experiment, the detector was exposed to a ^{252}Cf neutron source 5 cm away in the direction away from the photomultiplier tube (PMT). This is in order to establish the location of the neutron capture feature in the detector response, as well as to obtain characteristic waveforms. As the composite detector consists of two materials with different light output responses and different scintillation spectra that may be detected with different efficiencies, the unit "n.c." is defined as the mean detected light output for neutron capture on ^{6}Li in GS20 glass. To measure the response of the detector to γ radiation, and to determine the γ rejection, the detector was exposed to a ^{60}Co 1-µCi source placed 105 mm from the detector for 24 h. The sources were removed and the background was measured for 24 h. This process is consistent with typical γ rejection measurements, for example those reported in Ref. [11]. The digitizer used was a 500-MHz, 14-bit CAEN DT5730, and data acquisition was performed using the ADAQ software [49]; however, only a 250-MHz sampling rate was used. Raw waveform data were collected, along with event timestamps. The raw waveforms were processed and PSP values were optimized using the tail-to-total pulse integral such that the figure of merit for the separation between neutron capture in glass and electron/proton recoil pulses in PVT is maximized. The figure of merit F is defined as [50]

$$F = \frac{\mu_g - \mu_p}{W_g + W_p}, \tag{2.11}$$

where μ_g and μ_p represent the mean PSP of the events depositing energy in the glass and PVT regions, respectively, and W_g and W_p denote the corresponding full-width half-maxima in the PSP distributions. The optimized total and tail integral limits

relative to the pulse peak are −20 to 280 ns for the total integral and 42 to 280 ns for the tail integral. These limits result in $F = 2.1$. The mean measured glass and PVT waveforms, along with tail and total integral limits used to extract those waveforms, are shown in Fig. 2.3.

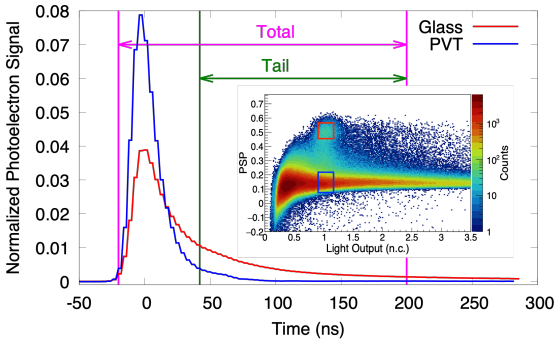

Figure 2.3: Averaged waveforms for the 7 wt.% GS20 composite detector with PSD and light output limits indicated (red and blue squares). Waveforms are averaged from 0.9 to 1.1 n.c. and a PSP of 0.45 to 0.55 for glass (red square) and 0.08 to 0.22 for PVT (blue square). The blue line represents a pulse which originates from an interaction in the PVT, while the red line represents a pulse which originates from an interaction with ^{6}Li glass. *Figure adopted from [2].*

These pulses represent two distinct event topologies illustrated in Fig. 2.2: a recoil region A and a capture region C. However, in addition, there is an intermediate region B representing events where electrons deposit their energy in both the PVT and glass, as shown in Fig. 2.4. The neutron capture region (region B) constitutes a 3σ ellipse in the light output/PSP parameter space, which is determined by fitting the ^{252}Cf experimental data to a 2D Gaussian function. This 3σ cut region is standard determining γ rejection in past work characterizing PVT and glass composite scintillators for high-γ backgrounds[1, 11, 45].

The γ rejection is defined as the ratio of number of γ rays misclassified as neutrons, *i.e.* those which fall in the neutron capture region, to the number of γ rays incident on the detector. In this work, a 3σ region that has been used in prior work such as [11, 33, 45] is used, which may be important in applications where the expected γ rate is far larger than the fast neutron rate such as in an active interrogation setting.

A typical requirement for γ rejection needed for safeguards applications is $<10^{-6}$ [51]. A smaller value of γ rejection ("better" γ rejection) is desired. For this particular detector, the γ rejection is 10^{-4} if the neutron acceptance is based on a 3σ Gaussian fit.

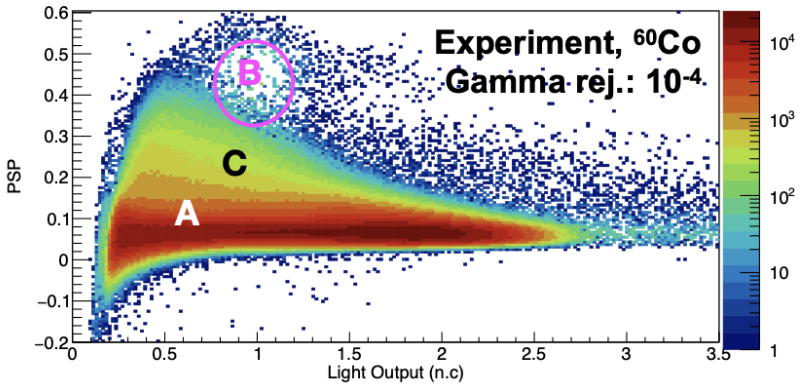

Figure 2.4: Detector response recorded for a 24-hour exposure of the 7 wt% shards detector to ^{60}Co radiation, with background subtracted. Region A is the PVT interaction region, Region B is the neutron capture region, and Region C is the intermediate region. *Figure adapted from [2].*

2.4 Geant4 simulation and construction of simulated waveform

The model described in Section 2.2 can be applied to energy deposition determined from a Geant4 simulation to calculate the PSP distribution and light output distribution for a simulated detector. Using this distribution, the same neutron capture region used in experiment can be applied to the simulated detector response, providing the γ rejection for a simulated detector. The process is outlined in this section when applied to the 500-µm, 7 wt.% shards case and can be adapted to other shards ^{6}Li and PVT composite detector designs.

A simulation of the interactions occurring in the detector was developed using Geant4. The dimensions of the detector in the simulation are the same as in the

experiment. The shards are modeled using 500-µm diameter spheres of ^{6}Li glass. The shards are randomly and uniformly distributed within the PVT cylinder. For the 7 wt.% case, approximately 8.2×10^4 shards are simulated. Each shard is placed at a position (r, θ, z) by sampling random numbers ξ_r, ξ_θ, and ξ_z from a uniform distribution ranging from 0 to 1 and then calculating (r, θ, z) such that

$$r = R\sqrt{\xi_r} \tag{2.12}$$

$$\theta = 2\pi\xi_\theta \tag{2.13}$$

$$z = Z\xi_z, \tag{2.14}$$

where R and Z represent the radius and the height of the scintillator, respectively. The shard locations are also tested for overlap with other shards and a new location is chosen should this be the case. For the simulation of irradiation, 10^6 γ rays from ^{60}Co (1173 and 1332 keV) are produced from a point source 105 mm away from the detector surface opposite to the one facing the PMT. Only events covering the solid angle extent of the detector were simulated. No other material is simulated other than the air surrounding the detector, and the simulation is run with a range cut of 1 µm, that is, a particle that stops after traveling less than 1 µm will not create further displacements (no additional particle tracks will be produced by the simulation as a result of electromagnetic interactions caused by that particle).

The energy deposited into glass and the PVT for each incident γ-ray event is extracted separately from the Geant4 simulation. From this, the fraction of energy deposited in the the ^{6}Li glass can be determined, as shown in Fig. 2.5. This parameter is the primary determinant for the resulting pulse shape and thus the event PSP.

Of all simulated events for the 7 wt.% loaded detector, 27 % of events exhibit some energy deposition in the glass.

To convert the deposited energy into light output, the fluorescence contributions

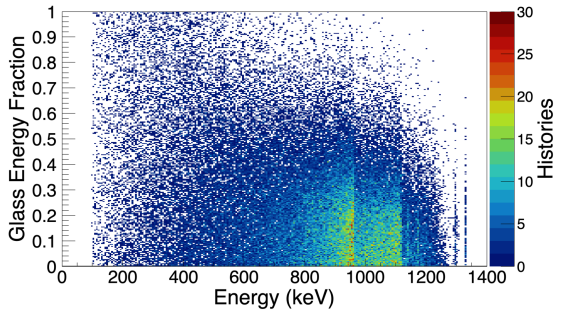

Figure 2.5: Fraction of energy deposited in glass for various total deposited γ-ray energies. Note that most events (73 %) have a vanishing glass deposition ratio, which is not shown since the plotted range for the fraction of energy deposited in glass is set to > 0. The features at 963 and 1118 keV are the Compton edges of the ^{60}Co energy deposition within the glass volumes; however, in experiment these features are broadened enough to not be discernible. *Figure adopted from [2].*

from the PVT (L^{PVT}) and the glass (L^{glass}) are added. This is done for each sample of the simulated waveform, as described by Eq. (2.1). The Geant4 simulation only models the energy deposition within the material, which must be converted to scintillation light output. Since only γ interactions are being simulated, it can be assumed that the light output scales linearly with the energy deposited[10]. However, the scintillation efficiency of glass is lower than that of PVT. To determine the total light output, we add the contributions from glass and plastic energy depositions:

$$\mathcal{L}(E_e, t) = \kappa_e^{\mathrm{glass}} E_e^{\mathrm{glass}} S^{\mathrm{glass}}(t) + \kappa_e^{\mathrm{PVT}} E_e^{\mathrm{PVT}} S^{\mathrm{PVT}}(t). \tag{2.15}$$

Here, $\kappa_e^{\mathrm{glass}}$ and κ_e^{PVT} can be determined by measuring the light output using common check sources (*e.g.*, ^{137}Cs and ^{60}Co) and comparing it with the measured light output from neutron capture in the composite scintillator. The $\kappa_e^{\mathrm{glass}}$ parameter is determined in an experiment using a separate 1-inch cylindrical detector composed of ^{6}Li glass, by referencing the light output to the neutron capture peak.

For each event, a waveform for the corresponding energy deposition was simulated and its PSP was calculated. The shape of the waveform was determined from weighted superposition of two canonical waveforms, $S^{\mathrm{glass}}(t)$ and $S^{\mathrm{PVT}}(t)$, one representing

the events which deposit energy solely in glass, and another representing events which deposit energy solely in the PVT. Both of these canonical waveforms represent idealized waveform shapes. The PVT representative waveform was obtained by taking the raw waveform data from the ^{60}Co experiment and averaging all waveforms with a PSP within 0.1 of the PVT event PSP and a light output between 0.9 n.c. and 1.1 n.c. The glass representative waveform was obtained by taking the raw waveform data from the ^{252}Cf experiment and averaging all waveforms within 1σ in the neutron capture island in the light-output/PSP space.

The result is an idealized waveform representative of a particular energy partition between glass and PVT. However, in order to correctly model a realistic PSP parameter, perturbations must be added to the waveform to account for electronic noise and other statistical effects. To achieve this, each individual waveform sample is convolved with a three-parameter function which is commonly used for broadening the simulated light output in organic scintillators to account for energy resolution [18]. The waveform perturbation model includes three parameters: α, β, and γ, which are related to three types of contributions: the α parameter accounts for position-dependent light transmission, the β parameter accounts for information carrier statistics, and the γ parameter accounts for light-independent electronic noise:

$$\delta L = L\sqrt{\alpha^2 + \beta/L + (\gamma/L)^2}. \tag{2.16}$$

Of the three parameters to be varied in the resolution model, γ is determined from the fluctuation of the experimental baseline for the first eight samples (24 ns) of the pulse. For the parameters α and β, a parameter search is conducted by sweeping their values through the range of $3 \times 10^{-11}\,\text{n.c.}^{-2} < \alpha < 3 \times 10^{-6}\,\text{n.c.}^{-2}$ and $1.8 \times 10^{-6}\,\text{n.c.}^{-1} < \beta < 1.8 \times 10^{-5}\,\text{n.c.}^{-1}$. The light output range between 0.9 n.c. and 1.1 n.c. was used to compare the simulation with the experiment; this range of light output is of interest

for γ rejection as it corresponds to the light output associated with neutron capture in GS20 glass. From this comparison, a sum-of-least-squares analysis was conducted in a parameter search of values of α and β, and the α and β values that returned the lowest sum of square residual were selected for the simulated waveform perturbation. This parameter search yielded the results $\alpha = 3 \times 10^{-8}\,\text{n.c.}^{-2}$, $\beta = 1.2 \times 10^{-5}\,\text{n.c.}^{-1}$ and $\gamma = 5 \times 10^{-3}$. Perturbations are introduced into the waveform for each time sample of the simulated waveform independently by sampling random numbers distributed in a Gaussian distribution with spread $\sigma = \delta L$. It should be noted that this model assumes that these values of α and β hold constant for detectors of this type and geometry but with different glass loadings. As only one loading of the geometry used was available, this assumption is made. The search of these parameters on a detector of the same type but different loading would be needed to verify this; in particular, it is possible that α may be affected by different ^{6}Li glass loadings as different glass loadings may affect light transmission.

An example of an ideal simulated waveform, along with a final waveform with perturbations added and the comparison with an experimental waveform, is shown in Fig. 2.6. Both the light output and tail-to-total PSP can be obtained from this simulated waveform in the same way that it was obtained in the experiment, and the simulated detector response can be represented in the light output-PSP space, as shown in Fig. 2.7. The simulated waveform which correlates to the appropriate PSP distribution exhibits a higher degree of perturbation, or "noisiness" than that measured in the experiment, as shown in Fig. 2.6. It is hypothesized that this discrepancy could be attributed to time-dependent factors outside the model described by Eq. (2.16), such as the gain variations of the PMT and granularity of pulse amplitude digitization. To alleviate this discrepancy and to further examine the appropriateness of the model, the effective time sampling rate of the simulation is reduced using a running average of 5 samples. This is done due to the light output model being primarily used to broaden

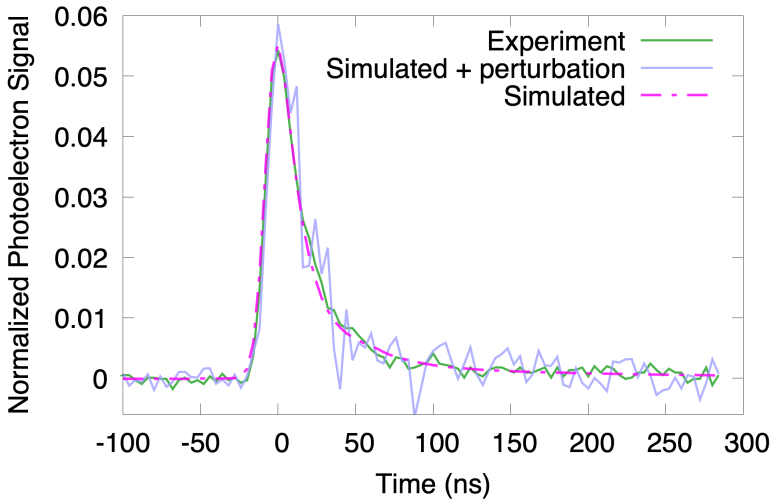

Figure 2.6: An example of an experimental waveform and simulated waveform ($PSP = 0.22$) with and without simulated perturbations. Waveforms are normalized such that the area under each waveform is 1. *Figure adopted from [2].*

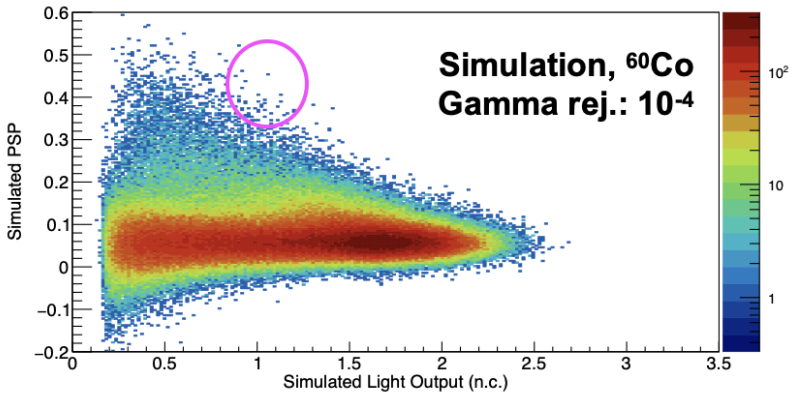

Figure 2.7: Simulated PSD plot for a 7 wt.% shards detector. The magenta circle denotes the neutron capture region within which γ induced events are deemed misclassified. *Figure adapted from [2].*

the light output for the entire pulse; this model may not be sufficient when attempting to model waveforms on a sample-by-sample basis. The resulting PSP parameters from the experiment can be compared to the simulation; a comparison of the PSP for a light output range of 0.9 to 1.1 n.c. is shown in Fig. 2.8. The quantity that is compared with the experiment is the γ rejection, which can be similarly determined in simulation by calculating the ratio of the number of γ events misclassified as neutrons (by appearing in the neutron capture region) to the number of simulated γ rays incident on the

detector. In this case, both the simulation and experiment have a γ rejection of 1×10^{-4}.

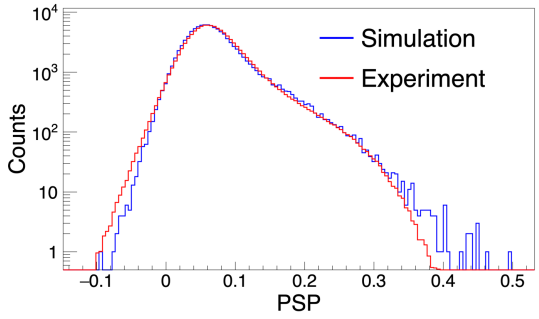

Figure 2.8: Comparison of simulation and experimental PSP distribution for light outputs between 0.9 to 1.1 n.c.. *Figure adopted from [2].*

To study the discrepancies between the simulated and experimental PSP distribution, several hypotheses may be formed and further studied by simulation. One possibility is the uncertainty in the shard loading during the manufacturing process, while another possibility are potential inhomogeneities in the distribution of shards.

2.5 Simulated effect of ^{6}Li glass shard loading and nonuniformity on γ rejection

Using the model described in Section 2.2 and implementing it using the results of simulation as described in Section 2.4, the dependence of γ rejection on shard loading can be simulated. A worse γ rejection due higher loading is found as a result. The simulated PSP distribution for the light output region is shown in Fig. 2.9. As expected, the PSP "tail" toward higher PSPs representing greater degrees of light production in ^{6}Li glass is evident. The effect of this phenomenon on γ rejection is shown in Table 2.1 – higher loading levels worsen the γ rejection.

Another possible explanation of the discrepancies in the PSP distribution in experiment and simulations is the presence of inhomogeneities in the shard distribution which can be introduced in the manufacturing process. The prior analysis assumes that

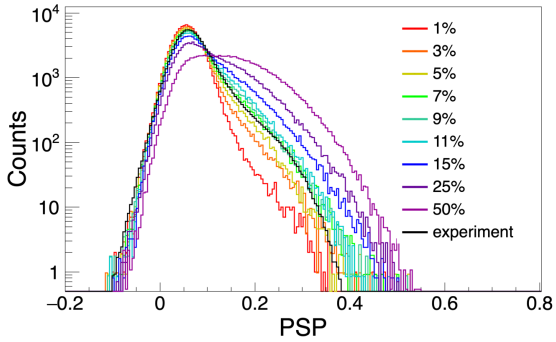

Figure 2.9: Comparison of different shard loading levels for light outputs between 0.9 to 1.1 n.c., for weight percentage of ^{6}Li glass loadings between 1 to 11 wt.%. *Figure adopted from [2].*

Table 2.1: Simulated effect of ^{6}Li shard loading on γ rejection. *Table adopted from [2].*

Loading (wt.%)	γ rejection
1	1.2×10^{-5}
3	2.4×10^{-5}
5	4.0×10^{-5}
7	1.1×10^{-4}
9	1.2×10^{-4}
11	1.8×10^{-4}
15	5.3×10^{-4}
20	1.3×10^{-3}
50	5.1×10^{-3}

the shards are homogeneously distributed within the detector. However, a deviation from homogeneous shard distribution may render a region of the detector more likely to exhibit partial energy deposition. To test the hypothesis that this effect can have the impact on the PSP distribution seen in the experiment, a limited study was conducted. In several simulations the shards distribution was skewed either to the center of the detector (inner biased) or on the perimeter of the detector volume (outer biased). The exact nature of such an inhomogeneity is unknown, so for investigation purposes, a simple linear bias is applied to the distribution of shards.

For this preliminary study, each shard is placed at a position (r, θ, z) where θ and z are sampled from uniform distributions as in Eqs. (2.13) and (2.14). Inhomogeneity

in the shards distribution is introduced using a parameter b, a bias parameter, where $b < 0$ denotes a bias toward the center, $b > 0$ denotes a bias toward the outer edge, and $b = 0$ represents a homogeneous case as in Eq. (2.12). We obtain the radial coordinate r of the shard by generating a random number ξ_r taken from a uniform distribution and calculating

$$r = \begin{cases} R\frac{1+b-\sqrt{(1+b)^2-4b\sqrt{\xi_r}}}{2b}, & b \neq 0 \\ R\sqrt{\xi_r}, & b = 0. \end{cases} \tag{2.17}$$

The resulting shard density using this method of biasing the shard distribution is illustrated in Figs. 2.10 and 2.11. The expected density in shards per mm^2 is

$$\rho(r^2) = \frac{N}{z}\frac{\mathrm{d}\xi_r}{\mathrm{d}(r^2)} = \frac{N}{z}\frac{(Rb+R-2br)\,(Rb+R-br)}{R^4}, \tag{2.18}$$

where N is the number of shards and z is the axial dimension (height) of the detector in mm.

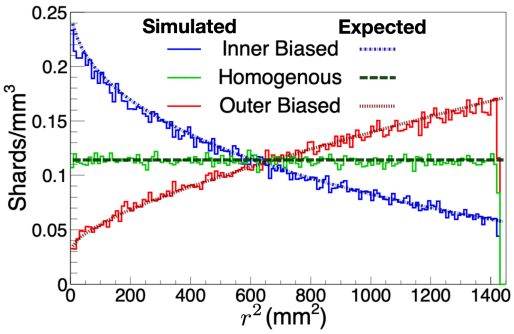

Figure 2.10: Volume density of shards for the inner biased, homogeneous, and outer biased case for a given value of r^2 as expected by the distribution, compared with the actual simulated distribution of shards. *Figure adopted from [2].*

The resulting PSP distributions for the homogeneous case detailed in previous sections, as well as inhomogeneities of bias $b = \pm 0.5$ either to the center of the detector or the perimeter, are shown in Fig. 2.12. Based on these results, it is possible to infer that the particular detector used in this experiment may exhibit inhomogeneities that

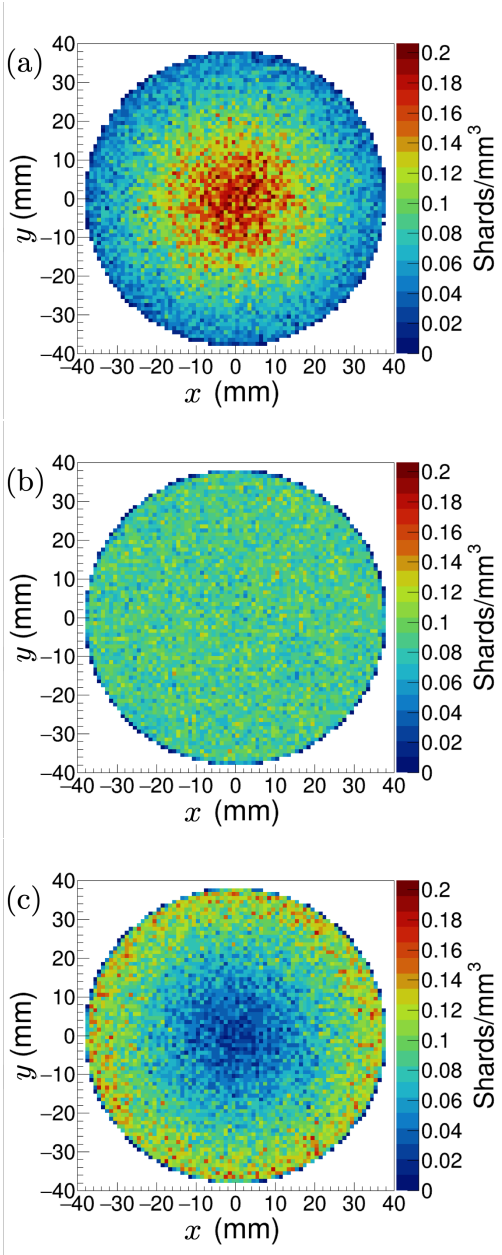

Figure 2.11: Illustration of three characteristic shard distributions: (a) inner biased ($b = -0.5$), (b) homogeneous, and (c) outer biased ($b = 0.5$).

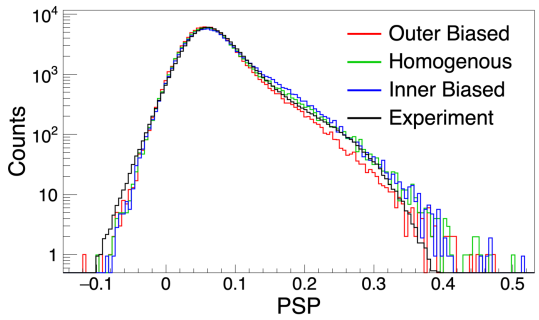

Figure 2.12: PSP distributions for light outputs of 0.9 to 1.1 n.c., for a homogeneous case as well as radially inhomogeneous cases. *Figure adopted from [2].*

are biased toward the outside edge of the detector given the inhomogeneities depicted in Fig. 2.12. However, a different nature of inhomogeneity may be present than the simple model considered here and give similar results. Further investigation into this effect can be undertaken in future studies and should be complemented by direct material characterization.

2.6 Conclusion

A model of energy deposition and resulting effect of γ rejection performance was established and used to simulate a heterogeneous ^{6}Li glass shard-loaded, PVT-matrix composite detector. The γ rejection predicted by simulation when the loading is 7% is 10^{-4}, consistent with the result obtained in the experiment. The effect of the shard loading was studied and yielded the expected result, where higher loading percentages of ^{6}Li shards increase the neutron detection efficiency but degrade the γ rejection performance.

A major area of future work would involve testing the assumptions made in the broadening of the waveform sampling. In this work, an assumption was made that the light output broadening parameters would be constant for this detector type with different loadings, as only one was available. For this, a detector of the same geometry and shard size but different weight percentage loading would need to be constructed

and tested.

The model does not match the experimental results exactly. It has been observed that the simulated waveforms exhibit a greater degree of noise between each time sample than that in the experiment. This may be attributed to effects that are not modeled by the light output model used to perturb the waveform samples, such as electronic noise. However, this sample-to-sample analysis is not of primary concern for determining the γ rejection, as the PSP only involves two broad integrals summed over several samples. Should there be an application for sample-to-sample analysis, exact waveform matching can be further studied.

The modeled PSP distribution at light outputs that are in the vicinity of light output produced by neutron capture on ^{6}Li in glass exhibits a slightly different shape from that seen in experiment. A preliminary study was conducted to show that a possible reason for this discrepancy is an inhomogeneous ^{6}Li shards distribution. A few possible variations of this inhomogeneity – situations where the ^{6}Li shards are more densely distributed at the center or the perimeter of the detector – have been studied and shown to have the corresponding effect on the resultant PSP shape. The model presented in this chapter could serve as a guide for optimizing the composite detector designs such that a favorable trade-off may be struck between the shard loading and neutron capture detection efficiency.

CHAPTER 3

Directionality from Neutron Capture through Bayesian Updating

3.1 Introduction

Capture-agent-doped organic scintillation detectors capable of identifying both neutron recoils and captures are a promising candidate for spectroscopy of low-energy neutrons via capture-gated spectroscopy [12, 43]. The addition of position sensitivity in these detectors has the potential to provide neutron directionality information, which could accelerate material localization in homeland security settings that may otherwise rely on proximity search. Position-sensitive organic scintillation detectors have been demonstrated and used as neutron scatter cameras [25, 26, 52, 53] as well as in near-field reactor antineutrino detection, where they have been shown to effectively reject backgrounds [30], which may allow for aboveground detector operation [30].

3.2 Scatter-Capture Fast Neutron Detectors

In an organic scatter-capture fast neutron detector, fast neutrons typically first undergo scattering on hydrogen and carbon nuclei. In the case a neutron loses most of its energy, which usually occurs through multiple scatters, the probability of its capture by a dopant with high neutron capture cross-section (*e.g.*, ^{6}Li, ^{10}B, or Gd)

greatly increases. In such detectors, scatter and capture events may be identified via a combination of pulse-shape and pulse-height discrimination, and capture-gated spectroscopy can be used to infer the incident neutron energy spectrum [12, 43]. The entire rapid thermalization chain is detected as a single pulse, as the amount of emitted scintillation light exhibits a correlation with the incoming neutron energy [43]. However, the thermalization light output is not linearly proportional to the neutron energy due to scintillator nonlinearity. The use of a capture signal also allows for the identification of neutron scattering events that would otherwise generate signals below the pulse-height-discrimination threshold, which is frequently limited by the PSD performance.

The kinematics of neutron scattering and the statistical properties of the subsequent diffusion and capture suggest an opportunity to extract the directionality of an incoming fast neutron. An illustration of the trajectory of a incoming fast neutorn upon a recoil-capture detector is shown in Fig. 3.1. Due to the conservation of energy and momentum, in neutron elastic scattering on a proton, the neutron scatters in the forward direction, *i.e.*, along the direction of the incident neutron. However, in scatter-capture detectors, the neutron typically scatters multiple times and diffuses in the detector volume before neutron capture occurs, which reduces the degree of correlation between the direction defined by the locations of neutron scatter and capture and the incident neutron direction. Still, a slight forward-capture tendency of the scattered neutron may provide some directionality information that supplements that obtained from the locations of single and multiple neutron scatters. In addition, in the case where the thermalization pulse is below the detection threshold but a subsequent neutron capture occurs, the occurrence of capture may improve the detection efficiency by identifying a neutron scattering event.

In a sufficiently large and efficient detector, crude directionality can be obtained even with the detection of a single scatter. Due to the attenuation of the neutron flux

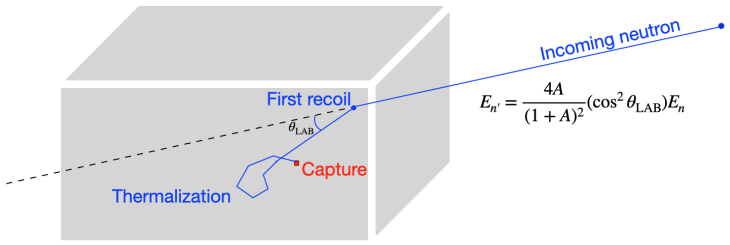

Figure 3.1: Illustration of the scatter-capture process.

by the detector, neutron scatters occur preferentially on the side of the detector facing the incoming neutron flux [25, 53].

3.3 Simulation in an ideal large spherical detector

To illustrate the basic principle on how directionality could be obtained with capture information, an idealized simulation was conducted with a pencil beam of DD neutrons (2.45 MeV) incident into a small aperture leading to the center of a large 1 m spherical detector, shown in Fig. 3.2. The large-size detector is meant to approximate an infinite detector where all of the energy of the neutron is deposited, eliminating the possible effect of geometrical effects in the detected event distribution. The detector is composed of polyvinyl toluene (PVT) homogeneously doped to 0.1 % by weight of ^{6}Li. The aperture allows the neutrons to travel to the center of the detector; the capture location is then registered relative to the weighted center of the scintillation signal that comprises the entire thermalization process. For this simulation, the incoming DD fast neutron originates at a polar angle of $\theta_n = 0°$, and interacts near the center of the detector.

The position of the neutron capture in spherical coordinates (r_k, θ_k, ϕ_k) is recorded, along with the position of the neutron recoil (r_r, θ_r, ϕ_r) The difference between the two points is referred to as the *recoil-capture vector* (r_x, θ_x, ϕ_x). The distribution of the polar component θ_x is shown in Fig. 3.4. As expected, there is a tendency for the

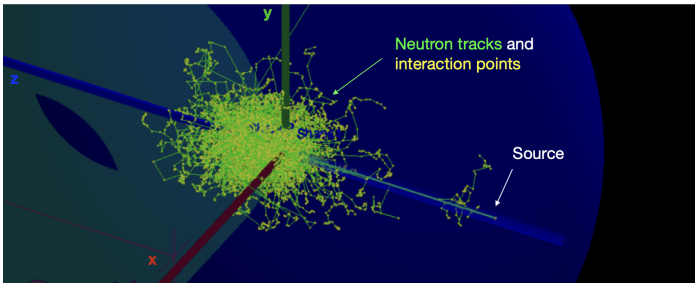

Figure 3.2: Geant4 rendering of idealized large-sphere simulation.

neutron to capture at forward angles, *i.e.*, along the direction of incident neutron flux.

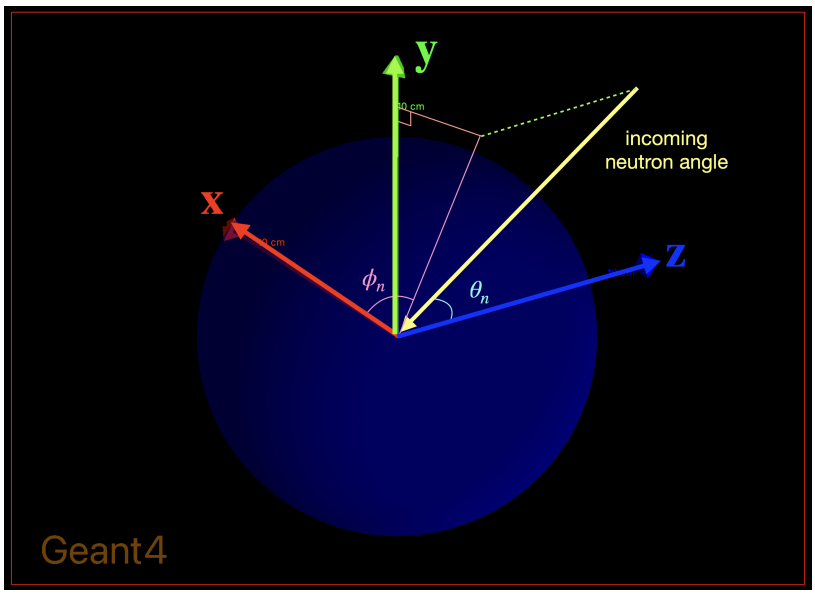

Figure 3.3: Schematic showing the θ_n and ϕ_n components of the incoming neutron angle **n**.

3.4 Bayesian Updating Methodology

An approach that makes use of Bayesian updating is used to estimate the incoming neutron angle from a combination of scatters and captures. For each neutron, the probability distribution of the incoming angle is updated regardless of whether the neutron undergoes only scattering or a combination of scattering and capture. To illustrate the process of Bayesian updating, one can take its most basic form: the goal is to determine which incoming neutron angle **n** is most probable given a certain event

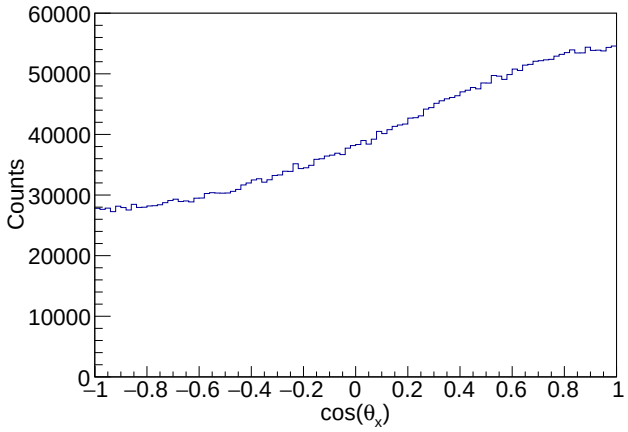

Figure 3.4: Distribution of $\cos\theta_x$, where θ_x is the polar angle subtended by the location of neutron capture relative to the weighted location of proton recoil in the detector shown in Fig. 3.2. A value of $\cos\theta_x$ closer to 1 represents a recoil-capture vector in the direction of the incoming neutron angle in this case.

topology, $[\mathcal{A}]$. In this work, the topology information used $[\mathcal{A}]$ includes information such as recoil position $\mathbf{r}$, a recoil-capture vector $\mathbf{x}$, and/or a light output cut. This probability, $P(\mathbf{n}|\,[\mathcal{A}])$, is given by the Bayes' theorem as

$$P(\mathbf{n}|\,[\mathcal{A}]) = \frac{P([\mathcal{A}]\,|\mathbf{n})P(\mathbf{n})}{P([\mathcal{A}])}. \tag{3.1}$$

Bayes' theorem is applied successively to the prior $P(\mathbf{n})$. When a new event is observed with topology $[\mathcal{A}]$, the prior is updated to the posterior using the likelihood of $[\mathcal{A}]$, $P([\mathcal{A}]\,\mathbf{n})$, which is simulated and used as a lookup table. From this, we obtain the posterior probability, $P(\mathbf{n}|\,[\mathcal{A}])$, updated after the first event. According to the principle of Bayesian updating, this posterior probability becomes the prior probability for the next event.

The incident neutron angle $\mathbf{n}$ is discretized, and $P(\mathbf{n})$ is initialized to a uniform distribution, as without any information we assume that every possible $\mathbf{n}$ is equally likely. This uniform distribution is the initial prior, $P_0(\mathbf{n})$. After observation of the

first event $[\mathcal{A}]_1$, the prior is updated to the posterior probability $P(\mathbf{n}|\,[\mathcal{A}]_1)$:

$$P(\mathbf{n}|\,[\mathcal{A}]_1) = \frac{P([\mathcal{A}]_1\,|\mathbf{n})P_0(\mathbf{n})}{P([\mathcal{A}]_1)}. \tag{3.2}$$

The new estimate is now $P(\mathbf{n}|\,[\mathcal{A}]_1)$. When another event is added, this new estimate becomes the prior $P_1(\mathbf{n})$ for the next iteration of Bayesian updating. In general, the prior $P_i(\mathbf{n})$ for the ith estimate takes into account all previous updates:

$$P_i(\mathbf{n}) = P\left(\mathbf{n}|\left\{[\mathcal{A}]_1 \cap [\mathcal{A}]_2 \cap ... \cap [\mathcal{A}]_i\right\}\right). \tag{3.3}$$

The next estimate $P_{i+1}(\mathbf{n})$ given a sequence of events with $\left\{[\mathcal{A}]_1 \cap ... \cap [\mathcal{A}]_2\right\}$ is

$$P_{i+1}(\mathbf{n}) = P\left(\mathbf{n}|\left\{[\mathcal{A}]_1 \cap ... \cap [\mathcal{A}]_{i+1}\right\}\right) = \frac{P([\mathcal{A}]_{i+1}\,|\mathbf{n})P_i(\mathbf{n})}{P([\mathcal{A}]_{i+1})}. \tag{3.4}$$

3.5 Application of Bayesian model to spherical detector simulation

3.5.1 Preparation of lookup tables

To apply the Bayesian updating method described in Sec. 3.4, a spherical detector with a diameter of 12.7 cm (5 inches) was simulated in the Monte Carlo Geant4 framework [48]. A spherical rather than a cylindrical geometry is used to minimize any effects from detector geometry. The size of the detector is larger than the one discussed in Section 2; a larger size is a better starting point as the attenuation through material would be more likely to yield directionality information in a larger detector. For the purpose of populating the lookup table, several simulations with discretized values of $\mathbf{n}(\theta_n, \phi_n)$ are used: the entire sphere in increments of 20 bins in $\cos\theta$ and 36 bins in ϕ. A plane source of incident ^{252}Cf neutrons is projected upon the sphere. For each $\mathbf{n}$, 10^6 incoming neutrons were simulated with a plane source

covering the cross-sectional area of the detector. A schematic showing the definition of the coordinate system is shown in Fig. 3.3.

For each incident neutron, the number of recoils and captures, the position of the neutron capture $\mathbf{x}$, the weighted position of neutron recoils $\mathbf{r}$, time to capture t, and energy deposited in the detector E are recorded. The light output from recoil L is estimated as [10, 54]

$$L = \sum_i L_i = \sum_i E_i^{3/2} \tag{3.5}$$

for each energy deposition i from neutrons scattering off protons. Other energy depositions such as scatters off of carbon are assumed to produce negligible light output. The direction of the weighted position $\mathbf{r}$ is used to account for energy deposition through scattering and is calculated as the mean recoil position, with each recoil weighted by the corresponding light output L:

$$\mathbf{r} = \frac{\sum_i \mathbf{r}_i L_i}{L}. \tag{3.6}$$

This simulation is used to prepare the following lookup tables:

A. $P([\mathbf{r}_i] \cap \{L > L_t\} \,|\mathbf{n})$, a recoil-only lookup table) above a discrimination threshold (2 dimensions, r_θ, r_ϕ)

B. $P([\mathbf{r}_i \cap \mathbf{x}_i] \,|\mathbf{n})$, recoil-capture lookup table (4 dimensions, $r_\theta, r_\phi, x_\theta, x_\phi$)

C. $P(\left[\mathbf{r}_i \cap \{\bar{x}\} \cap \{L > L_t\}\right] |\mathbf{n})$, recoil lookup table given no capture and light above a threshold (2 dimensions, r_θ, r_ϕ), and

D. $P(\left[\mathbf{k}_i \cap \{\bar{r}\} \cap \{L < L_t\}\right] |\mathbf{n})$, capture location lookup table given no recoil above a detection threshold is detected (2 dimensions, k_θ, k_ϕ).

Lookup tables are generated for each incident angle $\mathbf{n}$; a lookup table is a normalized

histogram of the recoil or capture distribution in $\cos\theta$ and ϕ. The histograms are binned with 4 bins in each dimension, shown in Fig. 3.5. Each bin represents a $P([\mathcal{A}]_{i,j}\,|\mathbf{n})$, with i, j being the indices of the bin of $\cos\theta$ and ϕ, respectively. Although increasing the number of bins per dimension could increase accuracy, doing so requires a longer simulation as the recoil-capture lookup table is 4-dimensional. Potential additional dimensions that could be used for future work include the radial component of each position (r_r and r_x), the light output L itself, or time to capture t, which were recorded but not used in this particular study.

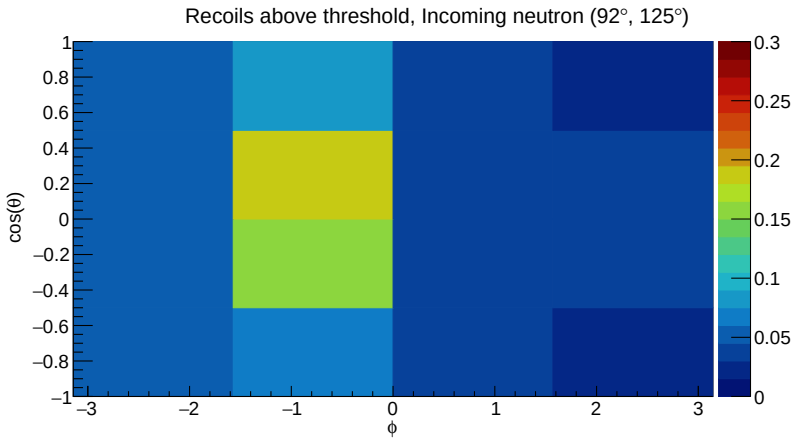

Figure 3.5: 4×4 recoil-only lookup table $P(\mathbf{r}|\mathbf{n} = [92°, 125°])$. The recoil-capture lookup table cannot be easily shown as it is in four dimensions.

This simulation is used to prepare lookup tables $P([\mathbf{r}_i \cap \mathbf{x}_i]\,|\mathbf{n})$ by histogramming the angular components of $\mathbf{x}$ and $\mathbf{r}$, effectively creating a four-dimensional lookup table spanning θ_r, ϕ_r, θ_x, and ϕ_x. In addition, an alternate lookup table $P(\left[\mathbf{r}_i \cap \{\bar{x}\}\right]\,|\mathbf{n})$ is used for recoil events that are not followed by capture.

3.5.2 Bayesian updating on small samples of incident neutrons

To test the Bayesian updating method, a Geant4 simulation with an identical setup was performed with a different seed. This was done for selected angles (ϕ_n, θ_n) consisting of pairs of 20 polar angles evenly spaced in $\cos\theta_n$ and 36 evenly spaced azimuthal angles. For each incoming neutron, Bayesian updating was performed. The

choice of the lookup table used is determined based on whether or there is a detectable recoil or capture. Light output information L is also collected for the simulation and an arbitrary threshold L_t can be set. Two different types of thresholds are studied. For the *discrimination threshold* $L > L_{t,\mathrm{disc}}$, a neutron capture enables the identification of a proton recoil that would otherwise be below the discrimination threshold. For a *detection threshold* $L > L_{t,\mathrm{det}}$, a neutron capture will not be able to do this since the proton recoil is not energetic enough to trigger the data acquisition system, and the recoil position is lost.

For a discrimination threshold, the process shown in Fig. 3.6 determines which $P([\mathcal{A}]\,|\mathbf{n})$ is used. If the neutron does not interact via proton recoil or capture, no updating is performed as no new information is provided (this is equivalent to multiplying by a flat distribution). Both a map of the single-event estimate and a cumulative estimate is obtained. For a *detection* threshold $L_{t,\mathrm{det}}$, the process shown in Fig. 3.7 is used.

To perform the Bayesian updating for each incident neutron indexed i, a cumulative Bayesian estimate map $P_i(\mathbf{n})$ is calculated. The map is initialized to a flat distribution:

$$P_0(\mathbf{n}) = \frac{1}{N}, \tag{3.7}$$

where N is the number of incoming neutron angles included in the lookup table; in this case, it is effectively a normalization constant. In this analysis, $N = 720$ for 36 values of n_ϕ and 20 values of $n_{\cos\theta}$. A single-event map $p_i(\mathbf{n})$ for an event indexed i is determined for each incident neutron interacting with the detector:

$$p_i(\mathbf{n}|\,[\mathcal{A}]_i) = \frac{P([\mathcal{A}]_i\,|\mathbf{n})}{P([\mathcal{A}]_i)} = \frac{P([\mathcal{A}]_i\,|\mathbf{n})}{\sum_{\mathbf{n}} P([\mathcal{A}]_i\,|\mathbf{n})}. \tag{3.8}$$

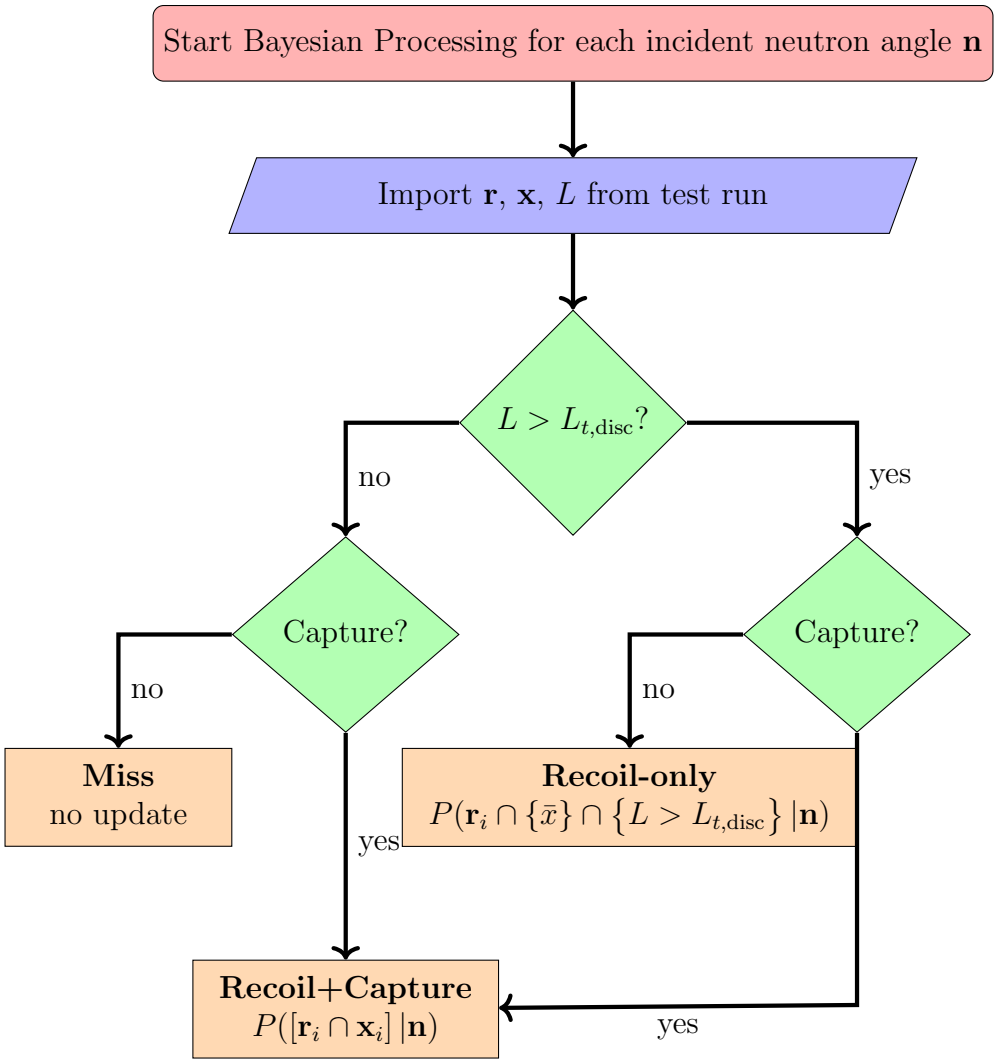

Figure 3.6: Flowchart for selecting a lookup table $P([\mathcal{A}]\,|\mathbf{n})$ for Bayesian updating executed for each incident neutron, with L_t being the *discrimination threshold*.

The cumulative estimate can then be found:

$$P_i(\mathbf{n}) = p_i(\mathbf{n}|\,[\mathcal{A}]_i) P_{i-1}(\mathbf{n}). \tag{3.9}$$

This iterative process produces an estimate that qualitatively becomes sharper with increased statistics, *i.e.*, with more incident neutrons. An example of a cumulative distribution along with its associated single-event estimate is shown in Fig. 3.8, where an expected value $\bar{\mathbf{n}}$ is calculated. Due to the spherical coordinates used to describe

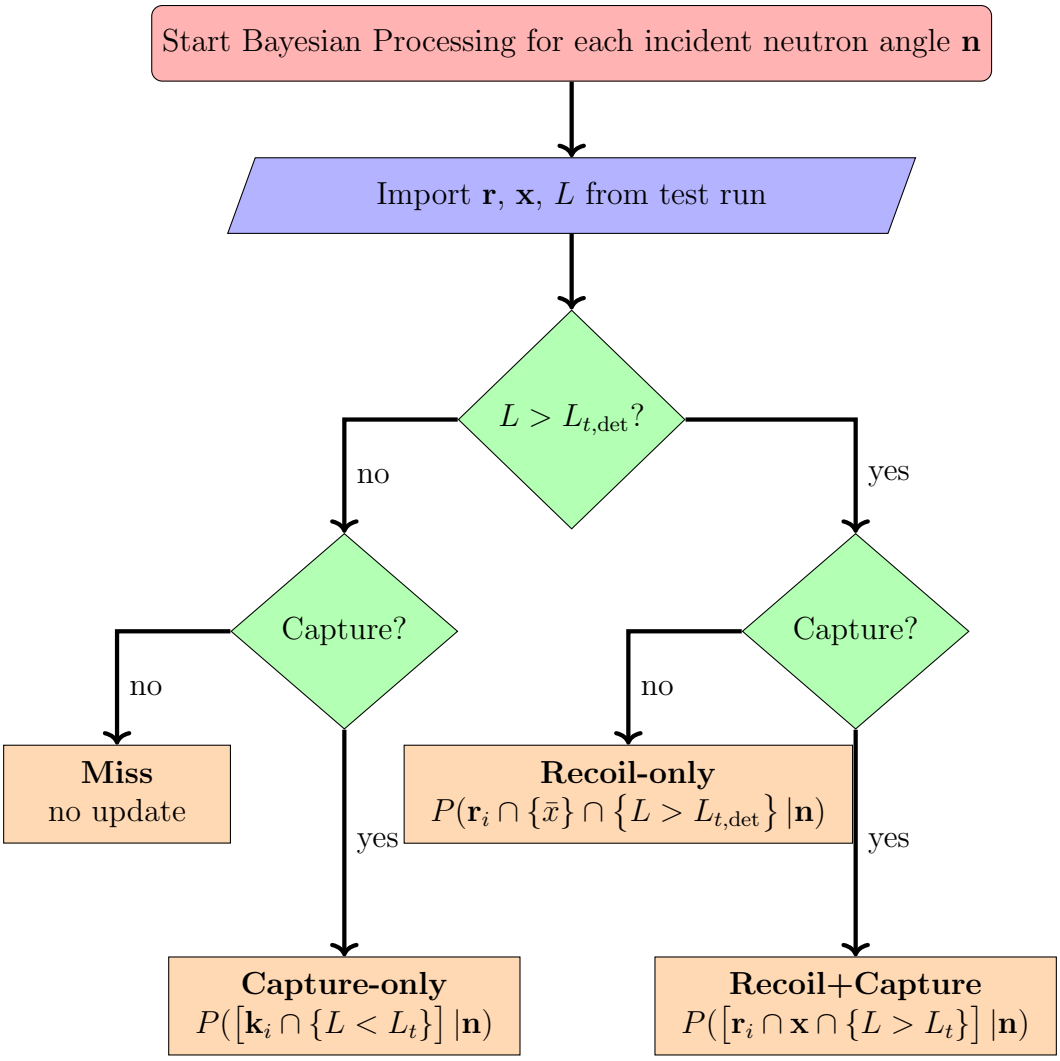

Figure 3.7: Flowchart for selecting a lookup table $P([\mathcal{A}]\,|\mathbf{n})$ for Bayesian updating executed for each incident neutron, with L_t being the *detection threshold*.

the incoming neutron angle, $\bar{\mathbf{n}}$ with components $(\bar{\theta}, \bar{\phi})$ is calculated in the following way:

$$\bar{\phi} = \arctan \frac{\sum_{\mathbf{n}} P(\mathbf{n}) \sin \phi_{\mathbf{n}}}{\sum_{\mathbf{n}} P(\mathbf{n}) \cos \phi_{\mathbf{n}}}, \tag{3.10}$$

$$\bar{\theta} = \arctan \frac{\sum_{\mathbf{n}} P(\mathbf{n}) \operatorname{sgn} \phi_{\mathbf{n}} \sin \theta_{\mathbf{n}}}{\sum_{\mathbf{n}} P(\mathbf{n}) \operatorname{sgn} \phi_{\mathbf{n}} \cos \theta_{\mathbf{n}}}. \tag{3.11}$$

The figure of merit for the quality of the estimate is the angular discrepancy ψ

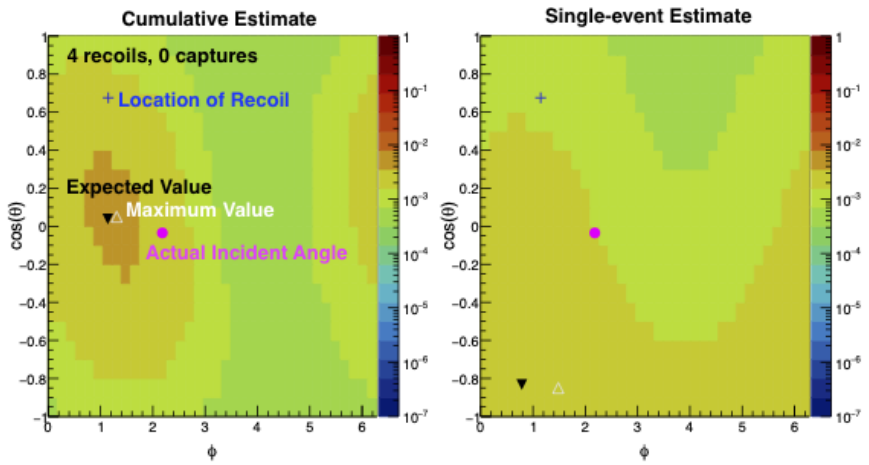

(a)

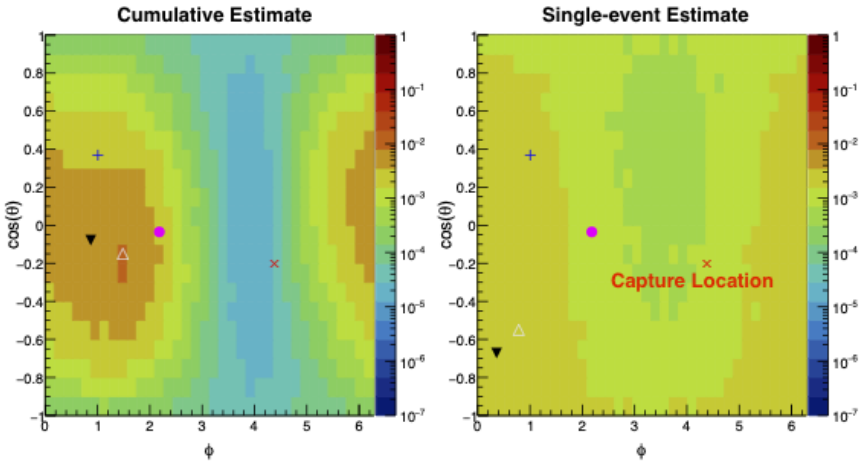

(b)

Figure 3.8: Examples of single-event Bayesian update estimate map for events with (a) proton recoils but no capture; (b) proton recoil followed by capture. Expected and maximum (bin with maximum value) are shown for reference.

Table 3.1: Number of recoils and captures for a given number of incident neutrons for the example shown in Fig. 3.9

Incident	Recoils	Captures
1	1	0
10	8	0
100	91	5
1000	853	77

between the estimate $\bar{\mathbf{n}}_i$ and actual incident neutron angle $\mathbf{n}_a$:

$$\psi \equiv |\bar{\mathbf{n}}_i - \mathbf{n}_a| = \arccos\left[\sin\theta_i \sin\theta_a \cos\left(\phi_i - \phi_a\right) + \cos\theta_i \cos\theta_a \cos\left(\phi_i - \phi_a\right)\right] \quad (3.12)$$

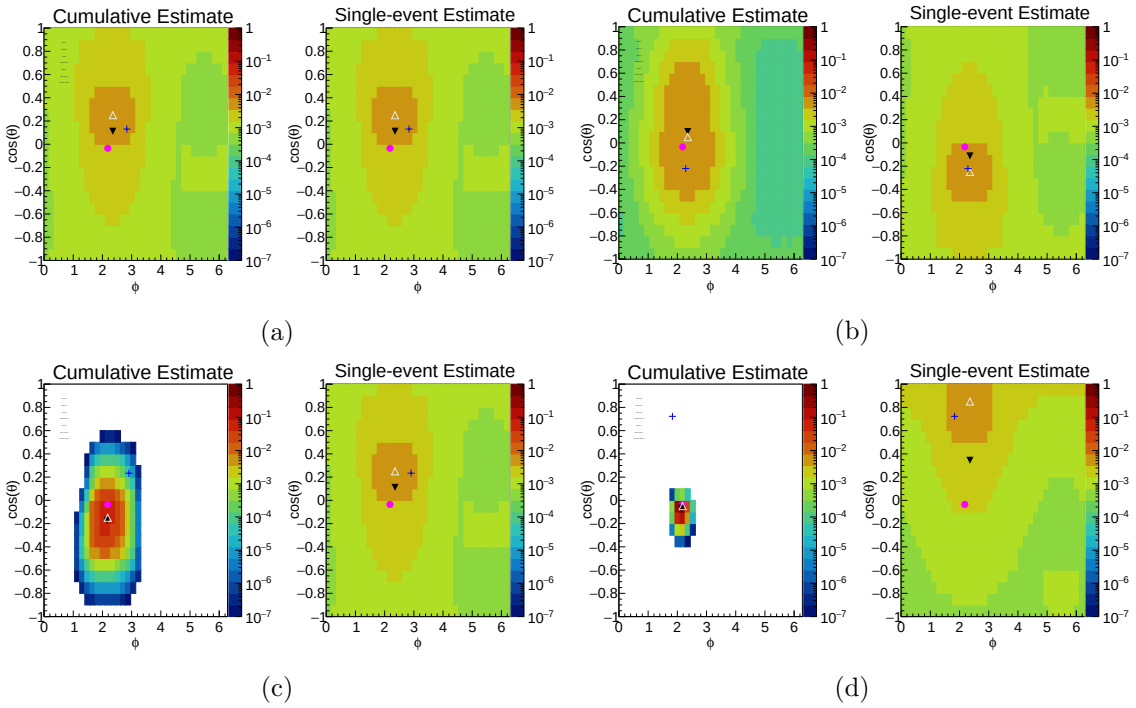

Figure 3.9: Bayesian estimated angle probability map after (a) 1; (b) 10; (c) 100; (d) 1000 incident neutron events (left), and single-event estimate for the associated incident neutron (left).

It is found that for the recoil-capture case, the lookup table has sufficient resolution such that each single-event estimate is not zero. For the recoil-only case, a lookup table of 4-bin resolution and an incident neutron count of 10^6 was sufficient for all thresholds. However, including capture information adds two additional dimensions, and thus a higher number of incident neutrons is needed for the lookup table.

There is a case where adding neutron capture information may be beneficial – that of high neutron/γ discrimination thresholds. In this case, a large fraction of recoil events may produce an amount of scintillation light that does not trigger data acquisition (detection threshold), or that is cut off in post-processing due to the inability to discriminate neutrons from photons (discrimination threshold). The advantage that the inclusion of capture may provide is that the neutron capture is usually easily identified by its consistent light output, and in heterogeneous composite detectors also by its distinct pulse shape [2, 18]. Using the capture information, the

preceding recoil may be identified even when it is below the discrimination threshold.

To study this condition, various thresholds were applied to the simulated light output L. The units of light output are arbitrary. Two light outputs are considered: a "low" threshold and a "high" threshold. These thresholds are shown in Fig. 3.10 together with the spectrum of ^{252}Cf for reference. The low threshold cuts exclude 36 % of incident neutrons with recoil events, and the high threshold cuts exclude 90 %. For each threshold, the lookup tables from Fig. 3.6 and 3.7 are regenerated. For the recoil-only case, only recoils that exceed the threshold contribute to the cumulative estimate.

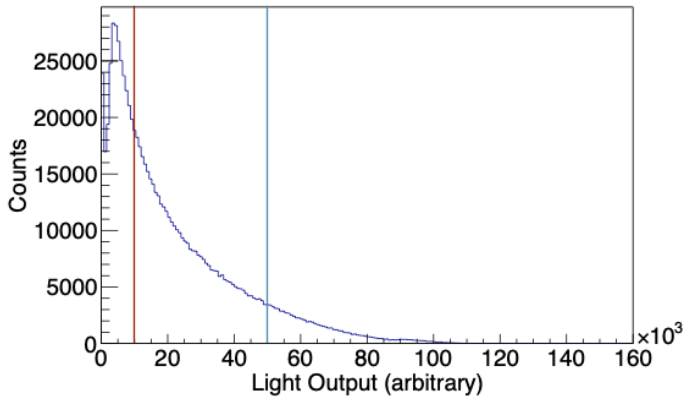

Figure 3.10: The low (red, 36 % cut) and high (teal, 90 % cut) thresholds used for studying the effect of thresholds on the Bayesian estimation method. The spectrum is simulated for a ^{252}Cf source.

The angular discrepancy, *i.e.*, the angle between the estimated and the actual incident neutron angle, decreases with a higher number of incident neutrons as shown in Fig. 3.11. Three cases are shown: recoil only, recoil with a detection threshold (recoil locations below threshold lost), and recoil with discrimination threshold (recoil locations below threshold recovered).

Especially for the low number of incident neutrons, there is great variation between different test trials of the Bayesian discrepancy progression, and conclusions cannot be drawn on the basis of a single test run. Next, several trial runs for the same **n** were conducted. The resulting average progression of the estimate with the number of

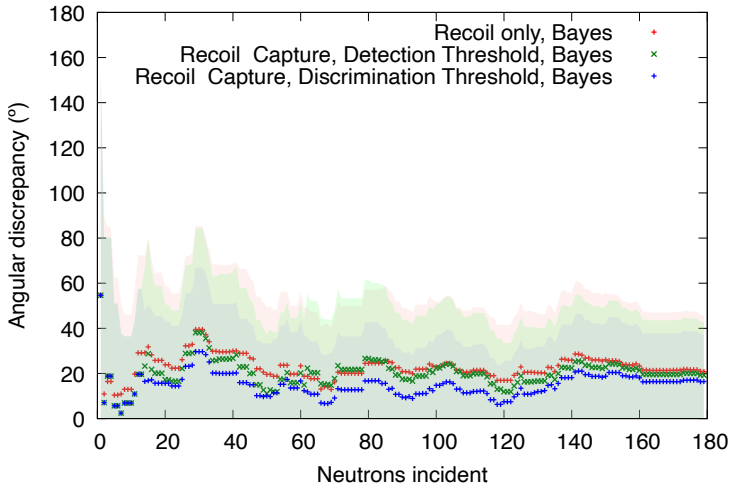

(a)

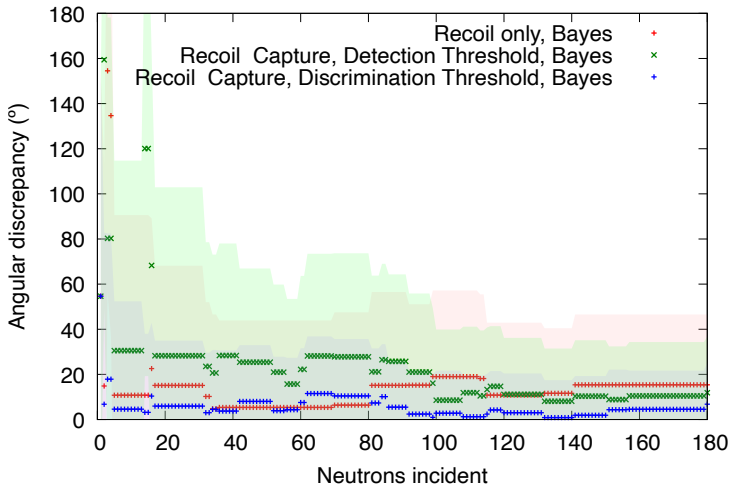

(b)

Figure 3.11: Angular discrepancy with an increasing number of incident neutrons for recoil only and recoil-capture with two different types of thresholds, (a) for the lower threshold and (b) for the higher threshold in Fig. 3.10. Shown is a single trial for $\mathbf{n} = (\theta = 92°, \phi = 125°)$.

incident neutrons is shown in Fig. 3.12. The resulting progression when the results of several discrepancy progression tests with different $\mathbf{n}$ are distributed across a range of angles (9 angles in $\cos\theta$ and 6 angles in ϕ) in 4π can be averaged, yielding the progressions shown in Fig. 3.13 For the low-threshold case, detected recoils greatly outnumber captures at approximately 10 recoils per capture, and thus the addition to capture in the model does not provide any significant benefit. However, when

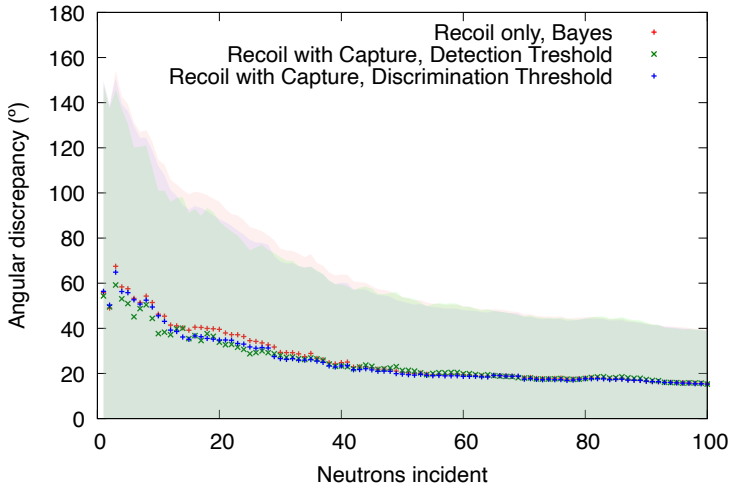

(a)

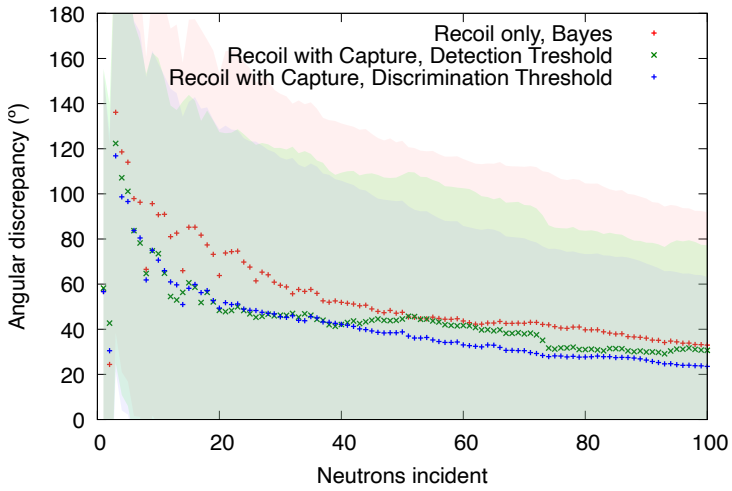

(b)

Figure 3.12: Angular discrepancy averaged across 100 trials with $\mathbf{n} = (\theta = 92°, \phi = 125°)$ when the light output thresholds shown in Fig. 3.10 are applied. (a) is the progression for low threshold, while (b) is the progression for high threshold.

most recoil neutrons are below a discrimination threshold, the recovery of information from such neutrons may improve the angular estimate for a fixed number of incident neutrons. Due to this effect only being apparent for the high-threshold case, it may be that the improvement in angular discrepancy can be attributed to the recovery of statistics rather than the capture being the cause of any improvement as predicted in Section 3.3. Ongoing work is being conducted to address this by implementing Bayesian updating to events where there is a recoil *and* a capture and comparing the

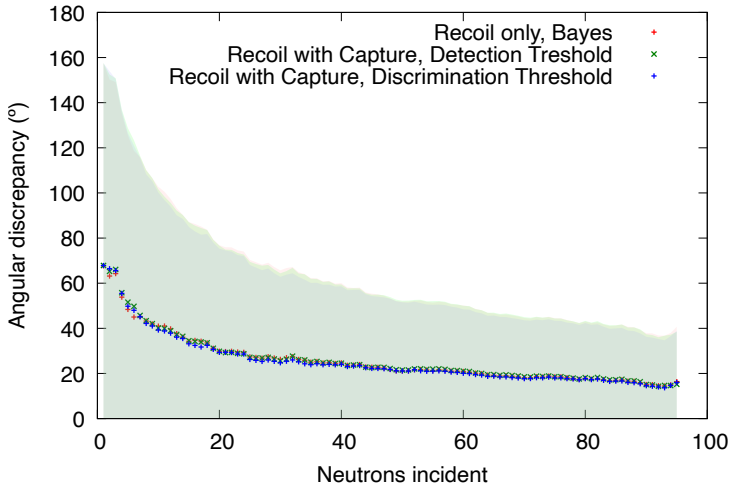

(a)

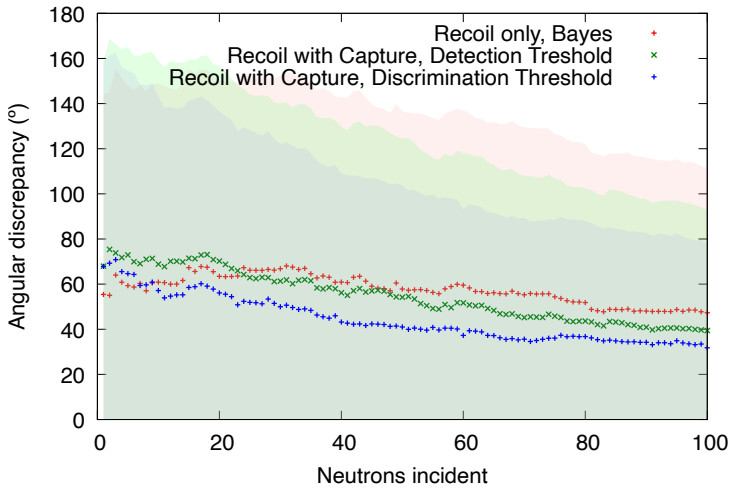

(b)

Figure 3.13: Angular discrepancy averaged over 54 different **n** when the light output thresholds shown in Fig. 3.10 are applied. (a) is the progression for low threshold, while (b) is the progression for high threshold.

result to a recoil-only case.

3.6 Conclusion

In this section, a Bayesian updating method was used to estimate incoming neutron angles given known recoil and capture locations, if present. Based on the comparisons between simulation test cases that ignore capture and cases where capture was factored

in shown in Fig. 3.12, there is no significant improvement in determining the direction of the incoming neutron, as measured by the difference between the estimated and actual incoming angles. However, in situations where a high particle discrimination threshold is set, recoil locations can be recovered, and in this case, the use of neutron capture can improve the angular estimate presumably due to the ability to recover lost recoil events. It cannot be yet concluded whether there is any improvement with capture beyond the recovery of lost recoils. One area of ongoing work is to find whether this improvement is specifically due to the addition of capture, or whether this improvement is seen solely due to the recovery of events that would otherwise be lost. This condition occurs when the number of neutron captures is comparable to the number of neutron scatters that yield light output above the discrimination threshold.

It is noted that the angular discrepancy does not converge to zero with additional incident neutrons. The exact cause of this is unknown and can be subject to further investigation. One possibility is the discrete selection of incoming neutron angles, although each bin would cover an equal area on the unit sphere, the angle between these selection angles is not evenly distributed.

Further study is recommended on this topic, including developing a better understanding of the effect of a realistic geometry and the nature of detector segmentation on directional neutron inference. The inclusion of other factors such as time to capture and light output can also be considered, but with the Bayesian approach, this would require more extensive computational resources for simulations due to the addition of extra dimensions in the lookup and test data sets.

CHAPTER 4

Application of an ASIC-based DAQ to a Neutron Scatter Camera

4.1 The TOFPET2 data acquisition system

New solid scintillation materials, including plastic [55–57] and glass [58], capable of discriminating nuclear from electronic recoils, are becoming available for radiation measurements in mixed neutron-γ fields. Scintillation detectors segmented into large numbers of channels are of increasing interest for fast-neutron detection, as they can record the location of interaction with high spatial fidelity, which can enable reconstruction of the source location and separation of signal from background. Segmented scintillation detectors have been implemented as single-volume scatter cameras [27], handheld dual-particle imagers [59], and arrays that can detect both neutron recoil and capture, making them potentially suitable for antineutrino detection via inverse beta decay [30]. To achieve high spatial resolution, silicon photomultiplier (SiPM) arrays are used because they combine many optical readout channels in a small sensor area and volume. One such system under development uses ^{6}Li -doped plastic scintillator and has been referred to as iSANDD [60]. A large number of signal channels requires a large number of DAQ channels, which has to date been associated with high cost, power usage, and technical complexity. These constraints may render a

system prohibitively large or expensive for use in portable devices for nuclear security measurements. However, it may be possible to overcome this limitation with compact ASIC-based DAQ systems. Most ASIC systems do not record full signal waveforms, which can make the discrimination between different types of interactions, *e.g.*, fast-neutron scattering and Compton scattering, challenging. One potential way around this problem is to split a signal into two channels and integrate them over two different periods. In this work, this method of PSD was performed on the TOFPET2, a DAQ developed for time-of-flight positron emission tomography [61–66]. By comparing the two time-integrated signals, PSD can be achieved [60, 67].

In this chapter, the charge collection characteristics of this particular ASIC were studied through a series of experiments. For the PSD study, the linearity and operating limitations were first studied by injecting a square electronic pulse input into the ASIC. In addition, the effect of integration time was tested using a tail pulser signal as input. These tests demonstrate the PSD capability using two different tail pulses. Following this, a test involving fast neutron scattering on a stilbene cube mounted directly to the SiPM array was used to investigate PSD when exposed to a mixed neutron/γ ^{252}Cf source.

4.2 TOFPET 2 Experimental Setup

The TOFPET2 is a commercially available ASIC developed by PETsys Electronics [31, 68] and is designed for use in positron-emission tomography medical imaging systems. This core application involves measuring 511 keV photons with scintillators such as LYSO or $LaBr_3$ with a time resolution of ~ 100 ps [31, 68, 69]. The TOFPET2 provides a time to digital converter (TDC) and charge to digital converter (QDC) mode and supports up to 64 independent channels per ASIC. In this work, the TOFPET2 ASIC evaluation kit [70] was used, which includes two FEM128 front end module (FEM)s with 128 channels each (two 64-channel TOFPET2 ASICs per

module), along with the necessary hardware and software for data acquisition running on a computer under the CentOS 7 Linux operating system. The components of the evaluation kit were adapted for use with an 8×8 pixel SensL J-Series 60035-64P SiPM. In addition to the standard evaluation kit, two custom components constructed by the manufacturer were used: a front end board (FEB) module that enables dual-output readout (FEB/S-2RO), which facilitates the duplication of SiPM signals, and diagnostic FEB with LEMO connectors (FEB/S-8L), which can be used to characterize the response of the ASIC to pulser signals. The FEB/D mezzanine is an interface that allows data from several ASICs to be processed and acquired. A diagram of the FEB/LEMO setup is shown in Fig. 4.2, while a photograph of the setup is shown in Fig. 4.1. A Peltier-based cooling system provided with the evaluation kit was refitted to a larger metal enclosure to accommodate the experimental setup.

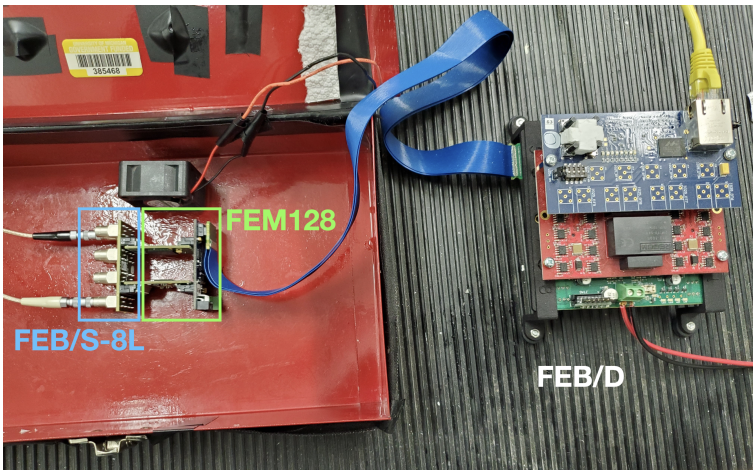

Figure 4.1: TOFPET2 arrangement used for pulser tests. The FEB/D interfaces with the computer via an Ethernet connection.

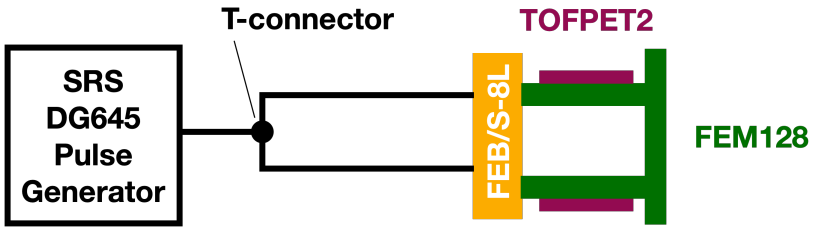

Figure 4.2: Diagram of setup for pulser experiments.

Before each experiment, a calibration process must be carried out which takes approximately 1.5 hours. The calibration is reset on every power cycle or when the temperature of the board deviates by 2 °C[71]. Notably, the baseline is determined once during calibration and for every pulse, so any baseline shifts cannot be adjusted on a per-pulse basis.

4.3 Measurement of ASIC Linearity with a Pulser

To characterize the ASIC's linearity and limits of operation, a Stanford Research Systems DG645 digital delay generator was employed to generate square pulses. To feed the signal to the ASIC, the pulser signal was split into two using a BNC coaxial cable T-junction and fed into the FEB/S-8L LEMO diagnostic readout board. The use of the T-splitter for the pulser is analogous to the use of the FEB/S-2RO board in a SiPM setup. The split signal is used to enable the measurement of pulse shape.

In communications with PETSys, it was stated that the maximum reliable integration time setting of the system was 421 ns. Nevertheless, integration time settings are apparently permitted in the range up to 1000 ns via software. In order to test the 421 ns limit and to determine what the response when the integration time is set to large values, 1 µs pulses (of between 120 and 1190 mV) were fed to the LEMO diagnostic board. Different amplitudes of square pulses with a length of 1 µs were used, this being far longer than any of the integration times that are tested. As shown in Fig. 4.3, there is evidence of saturation when the set integration time is above approximately 500 ns. As these saturation features occur at the same integration time despite varying amplitude, it can be concluded that this effect is caused by a limitation in the integration time setting rather than charge collection.

Next, the linearity of the ASIC was tested, also using 1 µs pulses but with a 421 ns integration time. This experiment establishes the charge collection limitations of the ASIC. The resulting linearity plot is shown in Fig. 4.4.

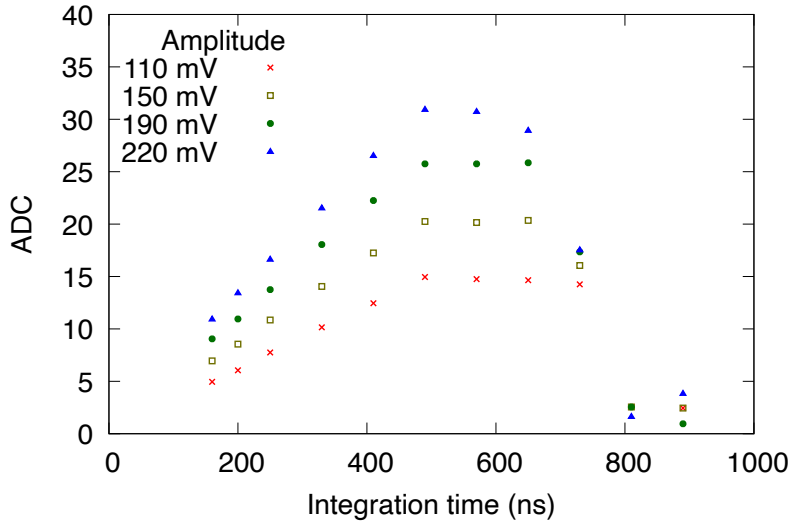

Figure 4.3: Single-pixel ASIC charge integration values (ADC) using 1 µs square pulses of varying pulse amplitudes, plotted as a function of ASIC integration time. Saturation effects arise due to limitations in integration time rather than in the total charge presented to the ASIC.

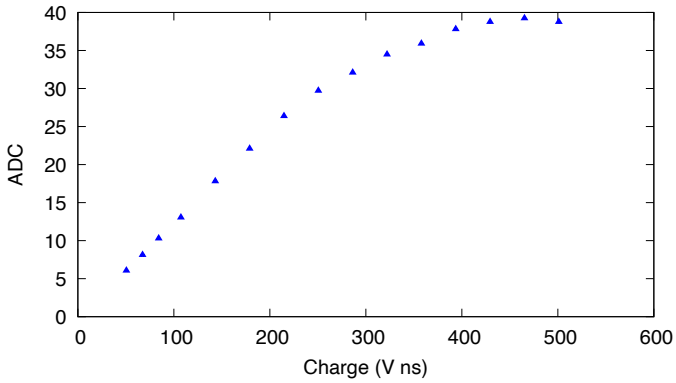

Figure 4.4: Linearity test of ASIC using 1 µs square pulses and 421 ns integration time. The charge shown is the product of the amplitude of the square pulse and the 421 ns integration time.

4.4 Tests of integration time characteristics of TOFPET2 using a tail pulser

To emulate the shape of a pulse reminiscent of one produced by a light sensor, a BH-1 tail pulse generator was used to conduct tests similar to that described in Section 4.3. Two decay times were used: 50 ns and 100 ns. The tail pulses were also

integrated using an oscilloscope output trace to calculate the charge in $\mathrm{V} \cdot \mathrm{ns}$. Like in the previous experiment with the square pulser, both the amplitude and integration time are varied, the amplitude from 50 to 400 mV, and integration times from 41 to 421 ns. The results of the linearity test are shown in Fig. 4.5. Significant nonlinearities are present for short integration times, below 50 ns. In addition, the ASIC integrates from the time the threshold is exceeded; this may cause a larger proportion of the pulse to be excluded from the integral for small pulses. The baseline is calibrated during the startup calibration stage rather than before each pulse; these two effects could contribute to unreliability at low integration times.

Following the linearity test for a single channel, a two-channel test was conducted to test the PSD capabilities. For this experiment, the same tail pulser was used to produce 50 and 100 ns pulses, also fed directly to the ASIC. The pulser output was split with a T-splitter and then fed into the FEB/S-8L LEMO connectors to the ASIC. As a demonstration of the most basic form of PSD, the pulser was initially set to a 50 ns fall time for 20 s, followed by an abrupt change to a 100 ns fall time setting. For this ASIC, the PSP is defined as in Eq. (1.7):

$$PSP = \frac{Q_l - Q_s}{Q_l}, \tag{4.1}$$

where Q_l is the charge collected from the channel with a longer integration time t_l, representing the "total" collected charge, and Q_s is the charge from the channel integrated over a shorter period t_s, representing the "head" of the pulse from threshold to t_s after the threshold. As per the usual convention, the pulse tail is used to calculate PSP rather than the pulse head, consistent with the definition of PSP in Eq. (1.7). For $t_l = 421$ ns and $t_s = 91$ ns, the observed PSP is shown in Fig. 4.6. The spread in PSP is much greater than expected from a tail pulser; this suggests that there will be a significant contribution of the ASIC to the uncertainty in PSP in an actual

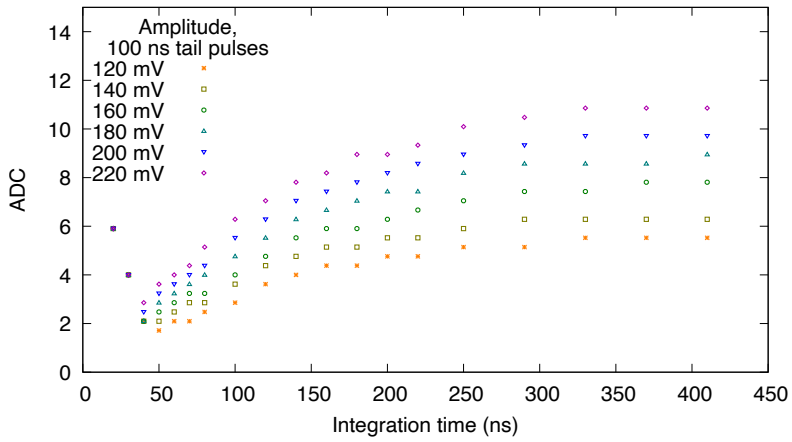

(a)

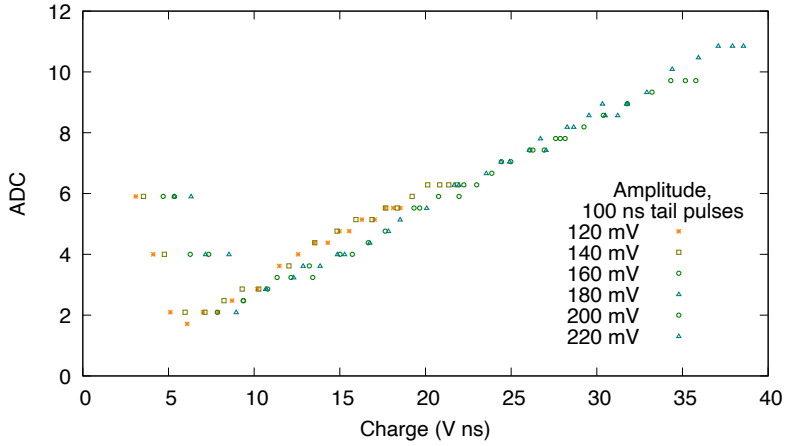

(b)

Figure 4.5: ASIC charge collection values (ADC) for 100-ns fall time tail pulses of varying amplitudes, when measured with integration times from 20 to 410 ns. The charge was measured by integrating oscilloscope traces. The data is plotted with respect to integration time in (a). The same data plotted against pulse charge is shown in (b). The ASIC charge collection for tail pulses is linear within this operating range.

detection application.

4.5 Single-pixel PSD with a Stilbene Crystal and SiPM Readout

To study a typical scenario for radiation detection with PSD, a 6 mm × 6 mm cube of stilbene was coupled to a single-pixel J-Series SiPM with a layer of optical

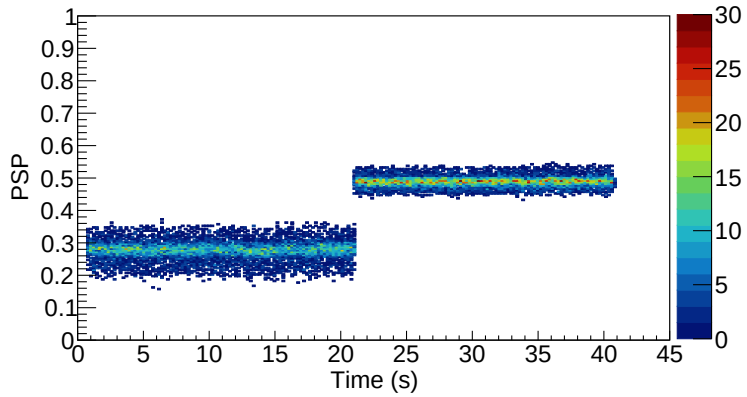

(a)

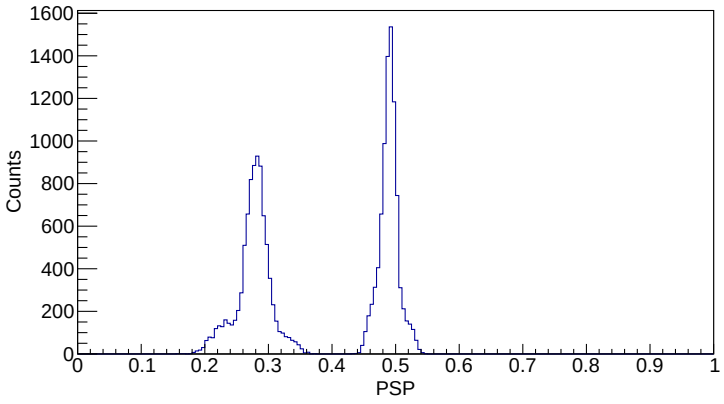

(b)

Figure 4.6: (a) PSD plot over time and (b) PSP plot measured using direct pulser feed into ASIC for 50 and 100 ns fall time pulses, with integration times $t_l = 421$ ns and $t_s = 91$ ns.

grease in between them. The stilbene cube was wrapped with Teflon tape on the sides of the cube not contacting the SiPM. The SiPM was then mounted to the custom FEB/S-2RO splitter board allowing each of the 64 pixels to be read out into two channels, resulting in 128 channels in total. The stilbene cube was exposed to several γ-ray sources, including ^{137}Cs, ^{22}Na, and ^{60}Co, to measure the response to γ radiation, DD and DT generators to measure the response to monoenergetic neutrons, and ^{252}Cf as a mixed source of broad-spectrum neutrons and γ's. The long integration time was set to 410 ns. The actual integration time as reported in the TOFPET2 data files is 11 ns longer than the set integration time, *i.e.*, 421 ns. Several head integration times

were tested to optimize the PSD: 71, 91, 131, and 171 ns (actual integration times as reported by the ASIC), and the results are shown in Fig. 4.7. The term *ASIC charge units* refers to the raw numerical output of the TOFPET2 that represents a quantity proportional to the collected charge.

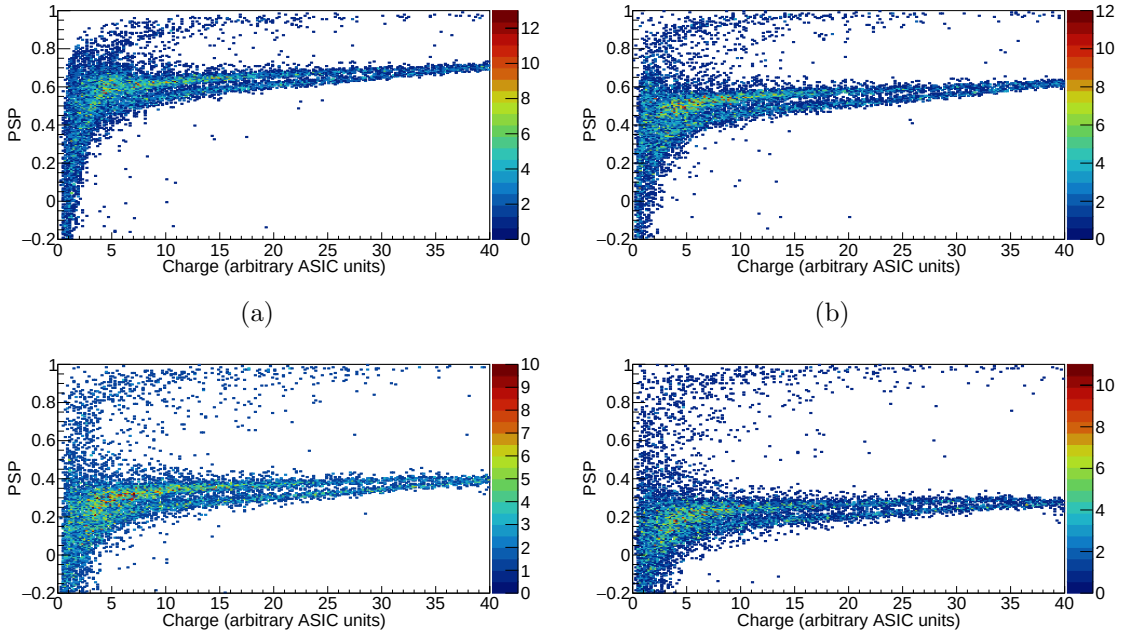

Figure 4.7: Tail/total PSD plots for head integration times of (a) 71 ns, (a) 91 ns, (a) 131 ns, and (a) 171 ns.

The PSD figure of merit, F, is defined as

$$F = \frac{\mu_\gamma - \mu_n}{w_\gamma + w_n}, \tag{4.2}$$

where μ_γ and μ_n are the mean PSP's, and w_γ and w_n are the full-width half-maximum (FWHM) of the PSP for γ's and neutrons, respectively. One notable feature of PSD is the deterioration of particle discrimination at higher charges and the drift towards higher PSP as the collected charge increases. The tail/total PSP distribution for a Pb-shielded ^{252}Cf source over a narrow light output range of 410 to 470 keVee is shown in Fig. 4.8.

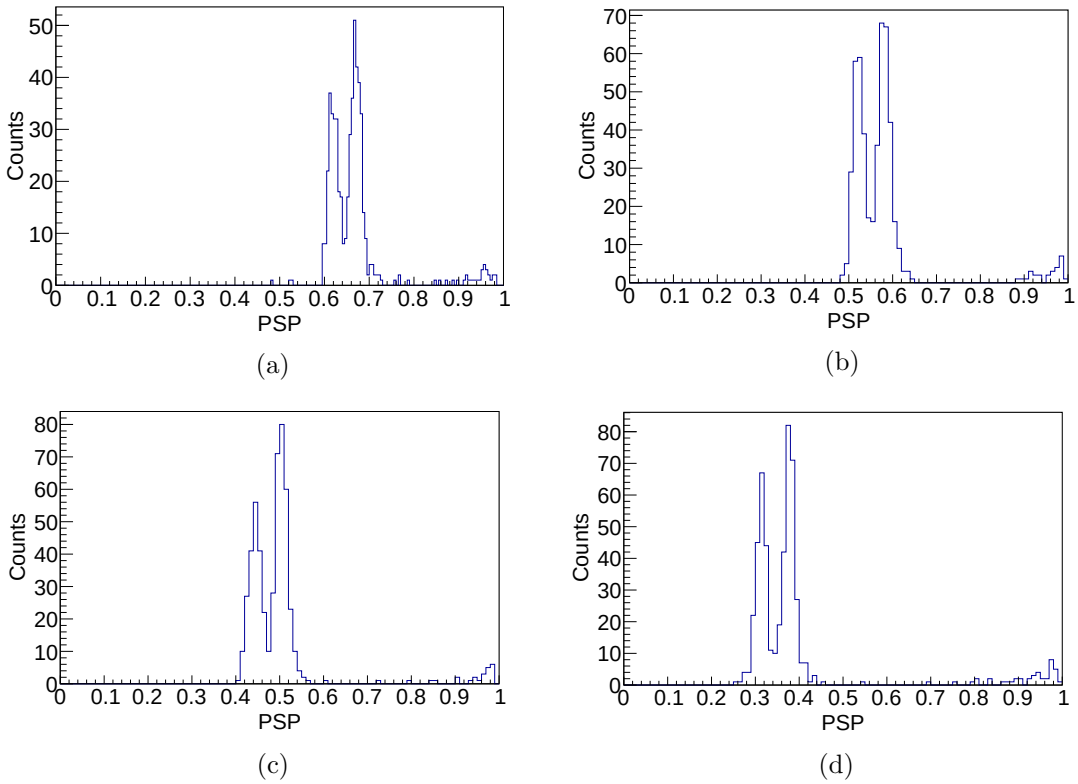

Figure 4.8: Tail/total PSP distribution for the light output range 410 to 470 keVee for (a) 71 ns, (b) 91 ns, (c) 131 ns, and (d) 171 ns.

The FOM of different charge collection bins is shown in Fig. 4.9. Rather than increasing as the collected charge increases, the FOM is highest at a head integration time of 131 ns and ∼20–25 ASIC charge units, with an FOM of 1.190, and then it decreases with increasing charge.

A possible reason for this behavior is the limited *total* integration time, which also must be optimized. Typically, for PSD optimization the total integration time should be as long as possible to encompass the entire pulse, but in the ASIC, due to saturation effects and degradation of linearity with very long integration times, only a part of the slowly decaying SiPM pulse is captured in the total integral. These nonlinearities are attributed to buffer overflows in the DAQ [71]. In the prior experiment, 410 ns was chosen as the integration time, because above that integration time, the charge collection linearity degrades and the system saturates. Improving the PSD over a wide

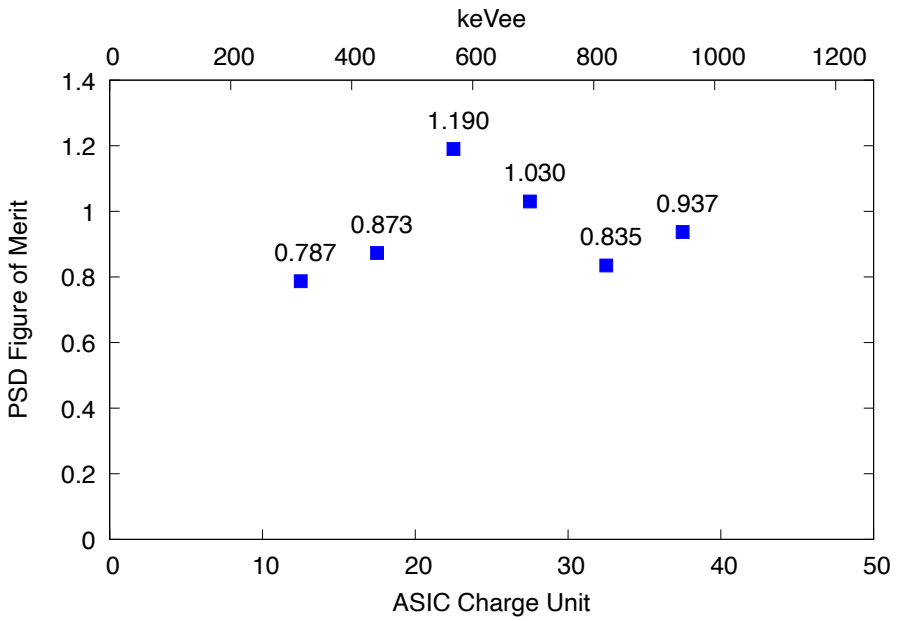

Figure 4.9: FOM for several ASIC-unit charge collection bins with a head integration time of 131 ns. Below ∼10 charge units and above ∼ 40 charge units, the two distinct pulse shape bands cannot be clearly resolved.

energy range is desirable, and if corrections for linearity can be made, the integration time may be extended to applications in which the light output is below approximately 10 MeVee.

A similar optimization scheme is used: rather than fixing the head integration time, the total integration time is modified. In this experiment, multiple measurements with a γ-ray source such ^{137}Cs must also be made to calibrate the charge scale to keVee, as the variation in the total integration time leads to different total charge collection values. In these runs, the head integration time is fixed at the value found to be optimal for the 410 ns total integration time and is equal to 131 ns (reported ASIC time).

The integration times that provide the best discrimination are then calibrated with a ^{137}Cs source, as the total integral cannot be directly prepared. These integration times are selected by finding the FOM of a charge range of ∼23–28 ASIC units, which is roughly the range that results in the best discrimination for all integration times.

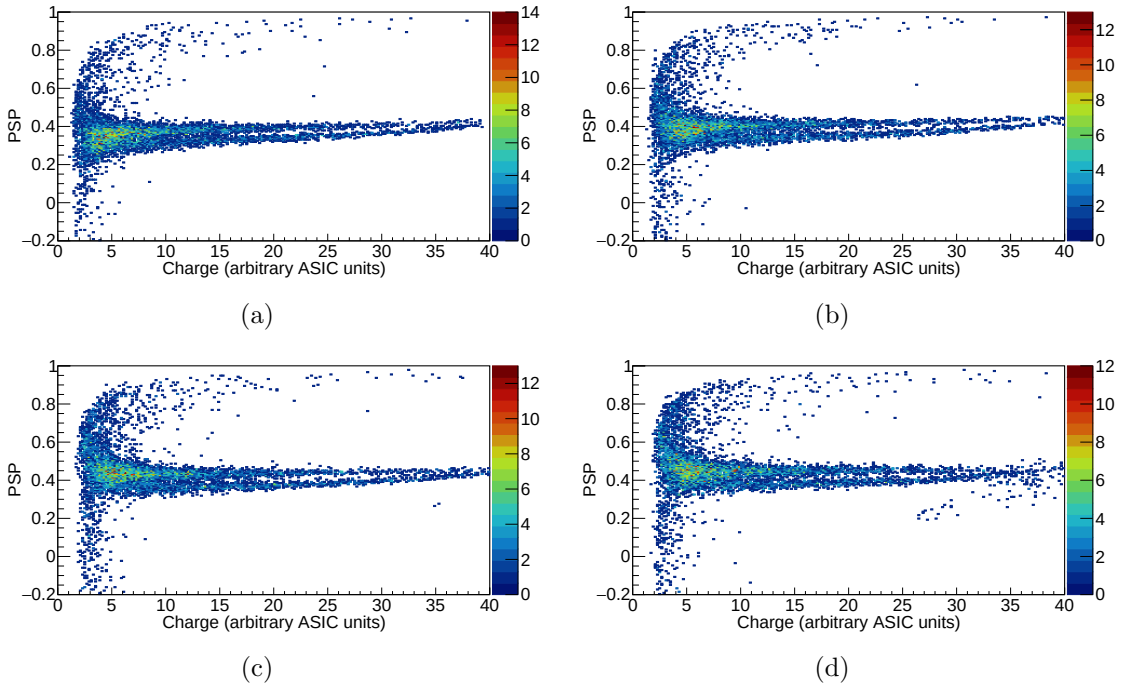

Figure 4.10: Raw tail/total PSD plots for total integration times of (a) 381 ns, (b) 421 ns, (c) 461 ns, and (d) 501 ns.

From this analysis, the total integration time of 461 ns demonstrated the highest figure of merit, 1.246.

4.6 Conclusion

Neutron detectors used in nuclear safeguards that use SiPM-based detector systems, especially neutron scatter cameras, could benefit from segmentation into hundreds of channels, which necessitates the need for high-channel-density and low-cost-per-channel data acquisition systems. However, the available compact systems lack full waveform digitization, and thus far PSD for identifying different particle types has been challenging. This work demonstrated PSD on a single channel of the TOFPET2 data acquisition system (PETsys Electronics), an ASIC-based data acquisition originally intended for positron emission tomography. A stilbene scintillator cube was placed on a pixel of a J-series SiPM with the TOFPET2 data acquisition and was exposed

to ^{252}Cf. PSD was achieved by splitting the SiPM signal into two channels and integrating the charge for a different duration for each of the channels. For a stilbene cube exposed with a ^{252}Cf source, a PSD figure of merit of 1.13 was achieved at 410 to 470 keVee with a short integration time of 131 ns and a long integration time of 421 ns. Gamma-only and neutron-only sources were used to verify that any PSD separation was indeed from different particle types: a PSP of 0.30 was observed with gammas and 0.37 was observed for neutrons.

CHAPTER 5

Calibration of the TOFPET2/SiPM System

5.1 Introduction

This work extends on the work of the previous chapter by introducing an LED calibration method, which is then applied to neutron and γ spectroscopy. The LED calibration is necessary to account for any nonlinearities in the ASIC/SiPM system. In this experiment, a SensL J-Series 60035-64P SiPM was illuminated with a pulsed light-emitting diode (LED) to develop a calibration curve that accounts for nonlinearities in the SiPM/TOFPET2 system. Finally, γ and neutron spectroscopy were demonstrated using a stilbene crystal attached to a single pixel of the SiPM exposed to various radioisotope sources and neutron generators. The light output spectra obtained from the TOFPET2/SiPM system exhibit shapes expected from γ rays and monoenergetic neutrons.

5.2 LED Linearity Experiments

In Chapter 4, linearity as a function of integration time (up to 421 ns) was investigated. In this chapter, the nonlinearities in the ASIC/SiPM system are assessed, and a calibration method is introduced to correct the nonlinearities to perform spectroscopy. A green LED was powered by a DG645 (Stanford Research Systems)

digital delay generator, and a DET36A (Thorlabs) photodiode was used to record the LED output. A J-Series SiPM was exposed to the LED light within a dark box using TOFPET2 for data acquisition. The SiPM was biased at 28 V, with 3.5 V overvoltage. The bias voltage was provided by the mezzanine board. A schematic of the experimental setup is shown in Fig. 5.1, while a photograph of the setup is shown in Fig. 5.2.

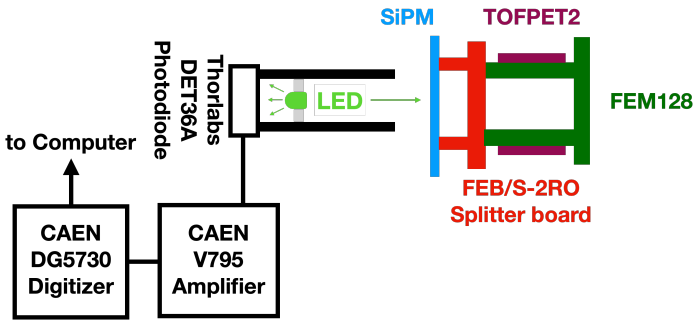

Figure 5.1: Illustration of the photodiode and SiPM setup used for LED-based calibrations.

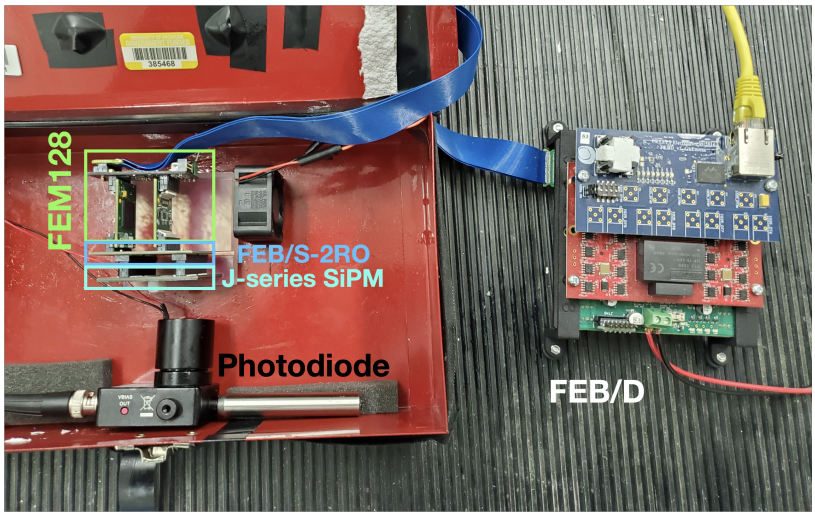

Figure 5.2: Experimental setup used for LED-based calibrations.

The ASIC output was compared to the signal measured by the photodiode in the setup shown in Fig. 5.1. Due to the relatively low sensitivity of the photodiode, the LED was placed in a lens tube pointing directly at the photodiode. The SiPM detects primarily reflected light. The amount of light received by the SiPM is far less than

but proportional to the amount of light incident on the photodiode. The photodiode pulses were amplified using a single channel of a CAEN V975 fast amplifier (10× fixed gain), as the unamplified photodiode pulses have too small amplitudes to be reliably collected with the desktop digitizer used. The amplified signal was acquired by a CAEN DG5730 desktop digitizer (14-bit, 500 MS/s), yielding raw waveforms of the photodiode signal, as shown in Fig. 5.3. These raw waveforms were baseline-subtracted using the first 16 samples, and the entire baseline-subtracted waveform was integrated in post-processing.

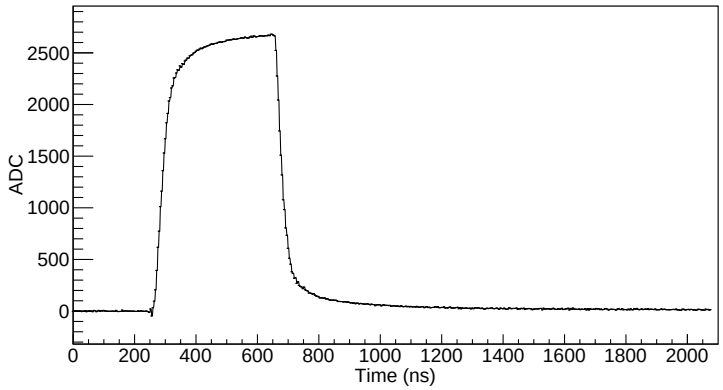

Figure 5.3: Example baseline-subtracted photodiode waveform from the CAEN DG5730 digitizer. In this example, the LED was driven by a 400 ns width, 5 V amplitude pulse.

The LED was powered using a Stanford Research Systems DG645 digital delay generator. Square pulses with amplitudes in the range of 1.3 to 5 V and pulse widths 50 to 400 ns were used to drive the LED, generating light pulses of different amplitudes and durations. The result using ADC values obtained from a single pixel of the TOFPET2 is shown in Fig. 5.4. The figure reveals several interrelated features. Above ∼20 ADC (TOPFET2 ASIC), the calibration curves deviate from each other depending on the width of the square pulse being fed to the pulse generator, and hence the length of the light pulse incident on the SiPM. As the TOFPET2 has no capability to digitize waveforms, the shape of the pulse that the SiPM/TOFPET2 system processes is unknown. Using this calibration, we can establish an operational range where

light measurements can be calibrated without correction for pulse shape. To fit the calibration curve, a function that describes the expected number of subpixels (SiPM microcells) triggered by a given number of incident photons is used [72]. The fitting of this calibration curve assumes only statistical effects, and does not consider aspects such as the dead time for any subpixel:

$$N_{\text{fired}} = N_{\text{total}} \left[1 - \exp\left(-\frac{\varepsilon N_{\text{incident}}}{N_{\text{total}}} \right) \right], \tag{5.1}$$

where N_{fired} is the number of subpixels triggered, N_{fired} is the total number of subpixels on each SiPM pixel, N_{incident} is the number of incident photons, and ε is the photon detection efficiency. The general shape of the nonlinearity can be described through compression losses in the SiPM [73]. These compression losses exist due to the overpopulation of single-photon avalanche diode triggers, a statistical effect caused by an excess of photons hitting the SiPM. However, this does not explain the dependence of the calibration curve on the pulse width, which we hypothesize to be caused by either the instantaneous charge capacity ASIC-based readout, or the re-firing of subpixels on the SiPM array. An experiment using a non-ASIC readout for the SiPM with a similar LED setup may be employed to find to which extent the latter hypothesis contributes to this effect.

In this particular experiment, there was no knowledge of the raw number of photo-electrons incident N_{total} or fired N_{fired}. Thus Eq. 5.1 is reformulated to be put in terms of the signal detected by the ASIC Q_{ASIC} and the signal detected by the photodiode $Q_{\text{photodiode}}$, leaving two free parameters A and B that can be fit with the calibration data, as in Eq. 5.2.

$$Q_{\text{ASIC}} = A \left[1 - \exp\left(-\frac{\beta Q_{\text{photodiode}}}{A} \right) \right], \tag{5.2}$$

Physically A is the expected ASIC analog to digital converter unit (ADC) value when all N_{total} subpixels are fired at once, and β is a scaling factor taking into account any scaling factors introduced by the photodiode ADC value and the detection efficiency of the SiPM:

$$\beta = \frac{A}{B}\varepsilon \tag{5.3}$$

where A is the same as before, ϵ is the detection efficiency and B is the expected photodiode/CAEN digitizer ADC value corresponding to the amount of light for which the all pixels of the SiPM fire. We fit this calibration curve for an operational range of below 20 TOFPET2 ADC, the fit shown in Figure 5.4. This range is chosen as it is only in this range where the pulse calibration curve does not depend on the pulse shape.

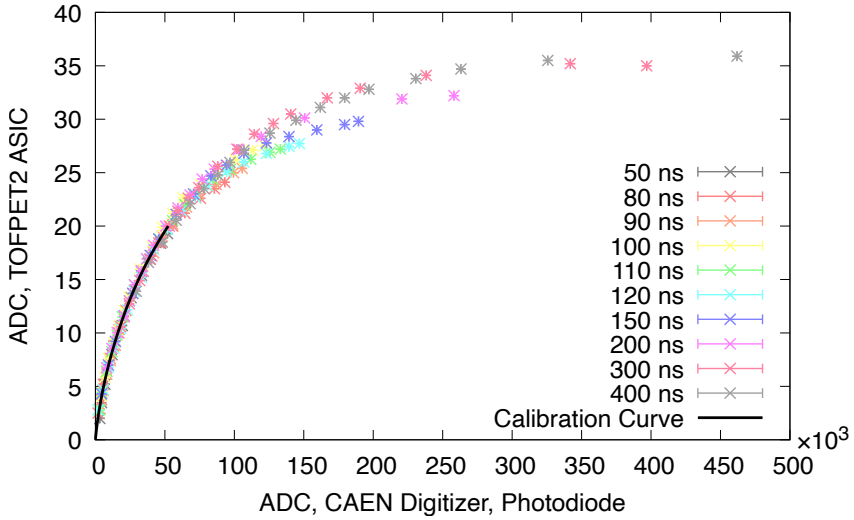

Figure 5.4: Single-pixel LED calibration curve for SiPM biased at 3.5 V overvoltage and coupled to TOFPET2.

For this particular case $A = 28.54$ ADC and $\beta = 6.90 \times 10^{-4}$. Note that these particular values are only valid to the particular setup described here, and is refitting is needed for each calibration.

5.3 Gamma and Neutron Spectroscopy with TOFPET2

Following the LED calibration, γ and neutron spectroscopy experiments were performed using a 6 mm cube stilbene crystal placed on the pixel for which the calibration curve was generated. The crystal was exposed to three γ sources: ^{22}Na, ^{137}Cs, and ^{60}Co. The Compton edge of ^{137}Cs and ^{22}Na were used to calibrate the energy scale. In addition, measurements were taken with two monoenergetic neutron generators manufactured by Thermo Scientific: a 2.45 MeV MP320 deuterium-deuterium (DD) fusion generator and a 14.1 MeV P211 deuterium-tritium deuterium-tritium (DT) fusion generator. A 1/4-inch sheet of lead was used to shield the stilbene crystal from ~50-keV photon radiation produced by the generator. To make the PSD cuts for neutron and γ radiation, a ^{252}Cf source was shielded with a 6.35 mm thin sheet of lead. The PSD cuts are then made to separate neutron and γ radiation, as shown in Fig. 5.5. The SiPM overvoltage setting is set to 3.5 V.

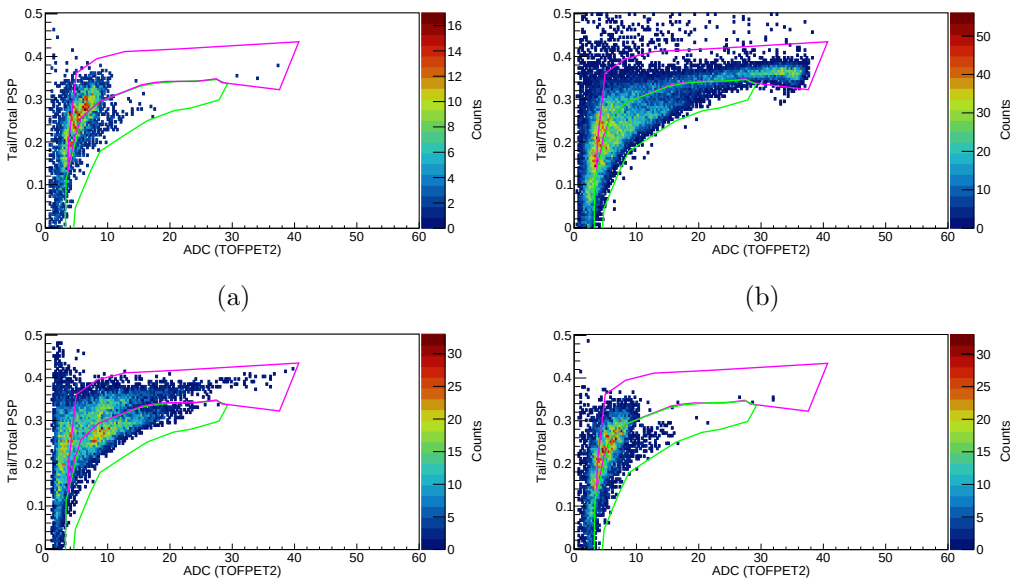

Figure 5.5: PSD plots for (a) a DD neutron generator, (b) DT neutron generator, (c) ^{252}Cf, and a (d) ^{22}Na gamma source taken by the TOFPET2.

These PSD cuts, shown in Fig. 5.5 are used to create uncalibrated neutron and γ

spectra, which are shown in Fig. 5.6. These PSD plots differ from the ones shown in Fig. 4.7 as the overvoltage to the SiPM used i this case is lower in this case (3.5 V for Fig. 5.5 and 5.5 V for Fig. 4.7.)

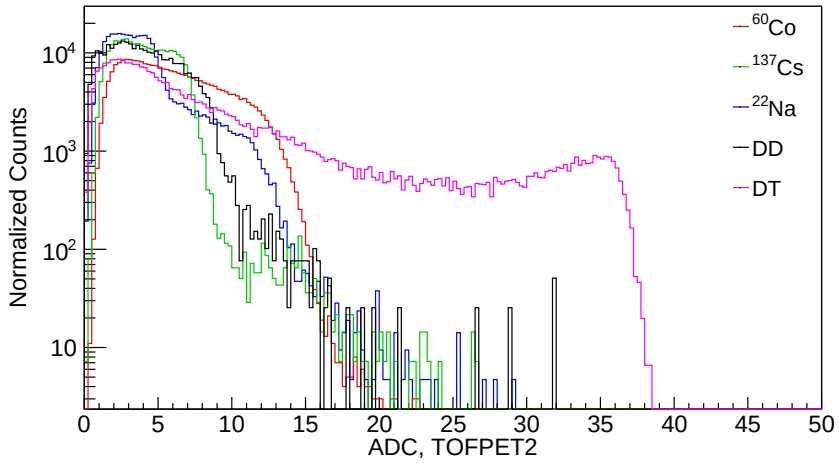

Figure 5.6: Raw TOFPET2 charge collection spectra for several γ and neutron sources.

Though an endpoint-like feature is observed with the uncalibrated DT spectra in Fig. 5.6, the location of the feature is beyond the operational range established by the calibration curve (below 20 ADC) and is therefore not considered reliable. In fact, the edge-like feature is most likely due to saturation.

To compare the performance of TOFPET2 to a typical data acquisition system, the SiPM and stilbene setup were read out using an ARRAYJ-60035-64P-GEVK breakout board manufactured by ON Semiconductor and a CAEN DG5730 desktop digitizer. The same single channel was read out in this experiment as in the case of the TOFPET2 experiment. The same DD and ^{137}Cs sources were used, and the resulting DD neutron spectra are compared against the TOFPET2 results in Fig. 5.8 to verify that the proton recoil quenching is consistent with expectations.

The proton recoil edge for incident DD neutrons corresponding to 2.45 MeV is 530 keVee, determined through a Gaussian fit on this edge, giving a quenching factor of 0.21. This result is consistent with the light output model for stilbene given by

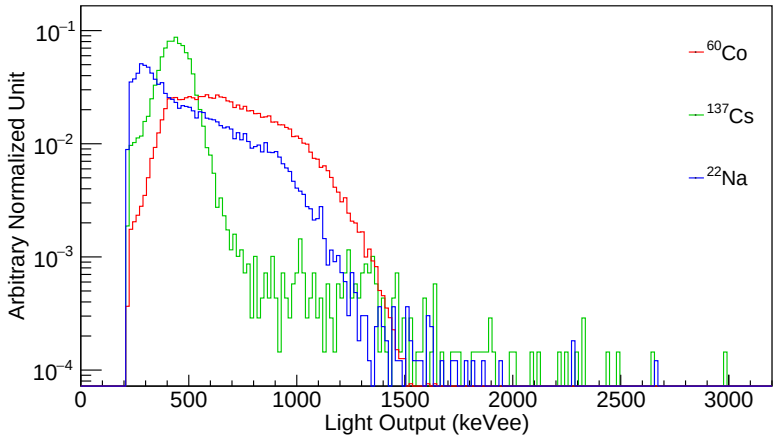

(a)

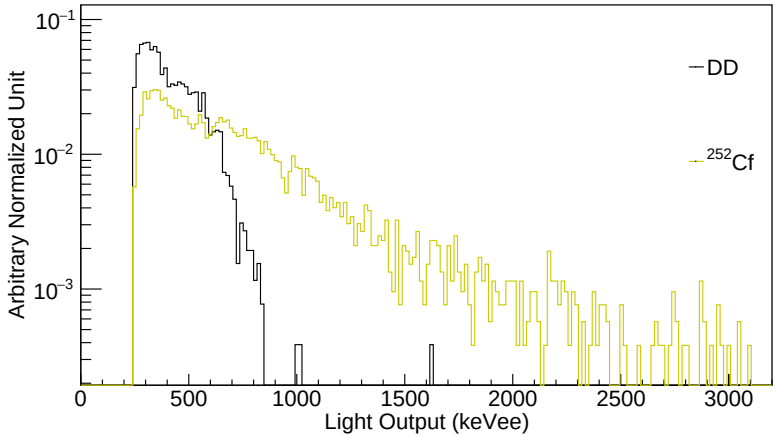

(b)

Figure 5.7: Calibrated spectra obtained from the TOFPET2 for a stilbene cube on a SiPM pixel for (a) γ and (b) neutron sources.

Ref. [74], which reports a light output of 535 keVee light output for a 2.45 MeV proton recoil in stilbene.

5.4 Conclusion

An LED calibration process was used to determine the linearity of the response of a TOFPET2 ASIC and SiPM-based detector system coupled to a 6 mm stilbene crystal. The SiPM channel output signal was split into two with a custom FEB/S-2RO splitter board, which is a method to achieve PSD. The operational limits of the TOFPET2

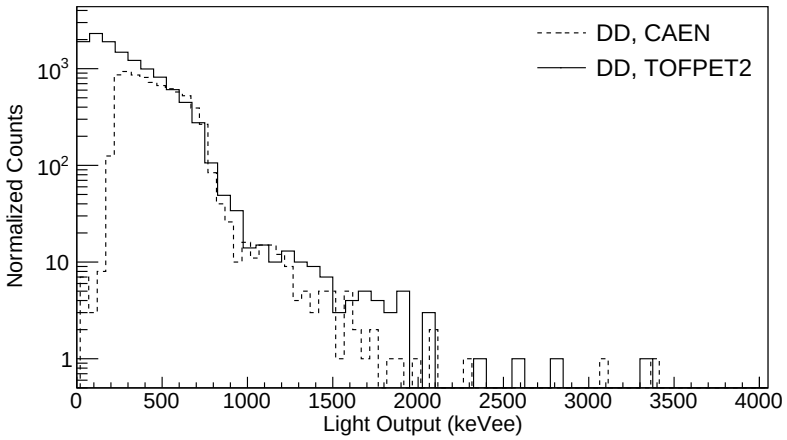

(a)

Figure 5.8: Calibrated DD neutron spectra measured with the TOFPET2 and a CAEN DG5730 desktop digitizer.

were studied with special attention to the integration time in a PSD setup using a pulser feed to the ASIC. After generating a calibration curve, output spectra for γ sources and a DD monoenergetic neutron source were generated by correcting for the nonlinearities in the system. As the light output produced by DT neutron interactions is too large, spectroscopy cannot be accurately calibrated for DT using this method due to the shape of the LED calibration curve as well as its dependence on the pulse shape for high-energy deposition. This calibration method suggests a rather limited dynamic range for neutron and γ spectroscopy. Improving the dynamic range of the ASIC would thus be desirable for future versions of the ASIC if it is to be used for γ and neutron spectroscopy. Topics suggested for further study include the investigation of the effect of lowering SiPM overvoltages and possible problems that may arise from such an approach, such as a degradation of energy resolution and PSD performance.

CHAPTER 6

Summary and Conclusion

6.1 Overview

This dissertation has focused on the methods to detect fast neutrons while capturing their directional information using organic scintillator arrays with an addition of a capture component. To accomplish this, advances are presented that improve the understanding PSD in scatter-capture detectors, provide the ability to reconstruct incoming neutron direction from the event topology recorded in the detector and examine the deployment and calibration of high-density data acquisition systems that do not employ waveform digitization.

In Ch. 2, the PSD characteristics of a heterogeneous recoil and capture detector were investigated through experiment and simulation. In such heterogeneous detectors, the existence of "composite" pulse shapes has been observed to affect γ rejection performance.

Following this, a new approach to estimate incoming neutron direction given from the positions of interactions in the detector was studied. A Bayesian approach was used to reconstruct an incoming neutron angle by constructing a lookup table compiled from a Monte Carlo simulation of a large number of neutrons incident onto the detector. Using this approach, it was determined that without a threshold below which recoils cannot be detected, neutron capture does not significantly improve the

estimate of the direction of the incoming neutron due to the much smaller number of captures when compared to recoils. However, in cases where PSD between neutrons and γ rays is poor and few neutron recoils can be identified as such, utilization of the neutron capture helps to improve the estimate of the incident neutron direction.

In a practical implementation of directional neutron detectors, a high-channel-density ASIC-based data acquisition system, TOFPET2, was investigated in conjunction with a generic neutron scatter camera. In Ch. 4, the performance of the ASIC was tested when in charge collection (QDC) mode. Rudimentary PSD was demonstrated with an electronic signal fed to the ASIC from a pulser. The PSD was subsequently demonstrated with stilbene exposed to a ^{252}Cf mixed neutron-γ source. Although PSD was observed, the PSD performance is significantly worse than that obtained with full waveform acquisition: a figure of merit (FOM) of 1.19 was achieved, whereas for full-waveform digitization of a 6-mm cube of stilbene coupled with a SiPM, a FOM of high has 1.37 [75].

A calibration method using an LED was investigated to enable neutron and γ spectroscopy in Ch. 5. A SiPM mounted to the ASIC readout was exposed to an LED, and the emitted light was also measured by a photodiode. From the combination of measurements, a calibration curve was constructed to correct the characteristics of the SiPM/ASIC system. However, the output as read out by the ASIC is dependent on the length of the LED pulse for large amounts of light detected such as scintillation produced by DT neutrons. Whether this is an effect of the ASIC or the SiPM is yet to be determined. Due to this effect, there is an operational maximum limit of 20 ADC units as reported by the TOFPET2 should this calibration method be used.

6.2 Future Work

The results of the work have the potential to be used in developing future neutron scatter-capture cameras. The simulation of neutron directional detection includes the

effect of segmentation and position resolution on the Bayesian analysis. In addition, the current analysis reconstructs the incoming neutron direction using the interaction position expressed as the angle measured in the coordinate frame referenced to the center of the detector. With a more extensive simulation, the Bayesian lookup table can be extended to the three-component location (including distance from the detector center) as well as other information that can be extracted from the detected event, such as scintillator light output and time to capture. Including this data in the Bayesian analysis is a potential direction for advancing this work. In addition, the implementation of machine learning is also a promising direction for the detection of neutrons with directional sensitivity [76].

Additional work would help improve the understanding of ASIC-based data acquisition. For the TOFPET2, the separation of effects introduced by the ASIC and by the SiPM light readout method is desirable to improve the calibration method and possibly extend the usable dynamic range. Beyond this, ASICs with waveform acquisition capability are in commercial development. The usage of compact ASIC-based data acquisition also has usage potential in other novel detector systems that require a large channel count, such as the LiquidO opaque scintillators [77, 78].

BIBLIOGRAPHY

BIBLIOGRAPHY

[1] A. Foster, A. Meddeb, K. Wilhelm, Z. Ounaies, and I. Jovanovic, "Characterization of lithium-glass and polyvinyl toluene heterogenous composites with varying geometries for fast neutron detection," *Nuclear Instruments and Methods in Physics Research Section A: Accelerators, Spectrometers, Detectors and Associated Equipment*, vol. 905, pp. 29–32, 2018.

[2] T. Wu, T. Shi, and I. Jovanovic, "Compound pulse characteristics of a heterogeneous composite scintillator in a gamma-ray field," *Nuclear Instruments and Methods in Physics Research Section A: Accelerators, Spectrometers, Detectors and Associated Equipment*, vol. 976, p. 164265, 2020.

[3] United States of America and Union of Soviet Socialist Republics and United Kingdom of Great Britian and Northern Ireland and others, "Treaty on the Nonproliferation of Nuclear Weapons," 1968. Accessed: 2023-01-26.

[4] H. R. 9757 - 83rd Congress of the United States, "Atomic Energy Act of 1954," 1954.

[5] J. Dolan, M. Marcath, M. Flaska, S. Pozzi, D. Chichester, A. Tomanin, and P. Peerani, "Active-interrogation measurements of fast neutrons from induced fission in low-enriched uranium," *Nuclear Instruments and Methods in Physics Research Section A: Accelerators, Spectrometers, Detectors and Associated Equipment*, vol. 738, pp. 99–105, 2014.

[6] A. Di Fulvio, T. Shin, A. Basley, C. Swenson, C. Sosa, S. Clarke, J. Sanders, S. Watson, D. Chichester, and S. Pozzi, "Fast-neutron multiplicity counter for active measurements of uranium oxide certified material," *Nuclear Instruments and Methods in Physics Research Section A: Accelerators, Spectrometers, Detectors and Associated Equipment*, vol. 907, pp. 248–257, 2018.

[7] F. Becchetti, R. Torres-Isea, A. Di Fulvio, S. Pozzi, J. Nattress, I. Jovanovic, M. Febbraro, N. Zaitseva, and L. Carman, "Deuterated stilbene (stilbene-d12): An improved detector for fast neutrons," *Nuclear Instruments and Methods in Physics Research Section A: Accelerators, Spectrometers, Detectors and Associated Equipment*, vol. 908, pp. 376–382, 2018.

[8] R. Chandra, G. Davatz, H. Friederich, U. Gendotti, and D. Murer, "Fast neutron detection with pressurized ^{4}He scintillation detectors," *Journal of Instrumentation*, vol. 7, p. C03035, Mar 2012.

[9] O. Searfus, K. Ogren, and I. Jovanovic, "Digital pulse analysis for fast neutron recoil spectroscopy with a ^{4}He scintillation detector," *Nuclear Instruments and Methods in Physics Research Section A: Accelerators, Spectrometers, Detectors and Associated Equipment*, vol. 1046, p. 167703, 2023.

[10] G. F. Knoll, *Radiation Detection and Measurement, 4th ed.* Wiley, 2010.

[11] M. Mayer, J. Natress, V. Kukhareva, A. Foster, A. Meddeb, C. Trivelpiece, Z. Ounaies, and I. Jovanovic, "Development and characterization of a neutron detector based on a lithium glass-polymer composite," *Nuclear Instruments and Methods in Physics Research Section A: Accelerators, Spectrometers, Detectors and Associated Equipment*, vol. 785, pp. 117–122, 2015.

[12] J. Nattress, M. Mayer, A. Foster, A. Barhoumi Meddeb, C. Trivelpiece, Z. Ounaies, and I. Jovanovic, "Capture-gated spectroscopic measurements of monoenergetic neutrons with a composite scintillation detector," *IEEE Transactions on Nuclear Science*, vol. 63, pp. 1227–1234, 2016.

[13] M. Smith, T. Achtzehn, H. Andrews, E. Clifford, P. Forget, J. Glodo, R. Hawrami, H. Ing, P. O'Dougherty, K. Shah, *et al.*, "Fast neutron measurements using cs2liycl6: Ce (clyc) scintillator," *Nuclear Instruments and Methods in Physics Research Section A: Accelerators, Spectrometers, Detectors and Associated Equipment*, vol. 784, pp. 162–167, 2015.

[14] N. D'olympia, P. Chowdhury, C. Lister, J. Glodo, R. Hawrami, K. Shah, and U. Shirwadkar, "Pulse-shape analysis of clyc for thermal neutrons, fast neutrons, and gamma-rays," *Nuclear Instruments and Methods in Physics Research Section A: Accelerators, Spectrometers, Detectors and Associated Equipment*, vol. 714, pp. 121–127, 2013.

[15] N. Zaitseva, A. Glenn, L. Carman, R. Hatarik, S. Hamel, M. Faust, B. Schabes, N. Cherepy, and S. Payne, "Pulse shape discrimination in impure and mixed single-crystal organic scintillators," *IEEE Transactions on Nuclear Science*, vol. 58, no. 6, pp. 3411–3420, 2011.

[16] J. B. Birks, *The theory and practice of scintillation counting.* Pergamon Press, 1967.

[17] F. Brooks, "Development of organic scintillators," *Nuclear Instruments and Methods*, vol. 162, no. 1-3, pp. 477–505, 1979.

[18] J. Nattress and I. Jovanovic, "Response and calibration of organic scintillators for gamma-ray spectroscopy up to 15-MeV range," *Nuclear Instruments and Methods in Physics Research Section A: Accelerators, Spectrometers, Detectors and Associated Equipment*, vol. 871, pp. 1–7, 2017.

[19] A. R. Spowart, "Energy transfer in cerium-activated silicate glasses," *Journal of Physics C: Solid State Physics*, vol. 12, p. 3369, aug 1979.

[20] F. Firk, G. Slaughter, and R. Ginther, "An improved Li6-loaded glass scintillator for neutron detection," *Nuclear Instruments and Methods*, vol. 13, pp. 313–316, 1961.

[21] E. Fairley and A. Spowart, "Neutron scintillating glasses part iii pulse decay time measurements at room temperature," *Nuclear Instruments and Methods*, vol. 150, no. 2, pp. 159–163, 1978.

[22] P. Marleau, J. Brennan, E. Brubaker, N. Hilton, and J. Steele, "Active coded aperture neutron imaging," in *2009 IEEE Nuclear Science Symposium Conference Record (NSS/MIC)*, pp. 1974–1977, 2009.

[23] I. Jovanovic, M. Heffner, L. Rosenberg, N. S. Bowden, A. Bernstein, D. Carter, M. Foxe, M. Hotz, M. Howe, A. Myers, and C. Winant, "Directional neutron detection using a time projection chamber," *IEEE Transactions on Nuclear Science*, vol. 56, no. 3, pp. 1218–1223, 2009.

[24] N. Bowden, M. Heffner, G. Carosi, D. Carter, P. O'Malley, J. Mintz, M. Foxe, and I. Jovanovic, "Directional fast neutron detection using a time projection chamber," *Nuclear Instruments and Methods in Physics Research Section A: Accelerators, Spectrometers, Detectors and Associated Equipment*, vol. 624, no. 1, pp. 153–161, 2010.

[25] J. J. Manfredi, E. Adamek, J. A. Brown, E. Brubaker, B. Cabrera-Palmer, J. Cates, R. Dorrill, A. Druetzler, J. Elam, P. L. Feng, M. Folsom, A. Galindo-Tellez, B. L. Goldblum, P. Hausladen, N. Kaneshige, K. Keefe, T. A. Laplace, J. G. Learned, A. Mane, P. Marleau, J. Mattingly, M. Mishra, A. Moustafa, J. Nattress, K. Nishimura, J. Steele, M. Sweany, K. Weinfurther, and K.-P. Ziock, "The single-volume scatter camera," in *Hard X-Ray, Gamma-Ray, and Neutron Detector Physics XXII* (A. Burger, S. A. Payne, and M. Fiederle, eds.), vol. 11494, p. 114940V, International Society for Optics and Photonics, SPIE, 2020.

[26] J. E. M. Goldsmith, M. D. Gerling, and J. S. Brennan, "A compact neutron scatter camera for field deployment," *Review of Scientific Instruments*, vol. 87, no. 8, p. 083307, 2016.

[27] K. Weinfurther, J. Mattingly, E. Brubaker, and J. Steele, "Model-based design evaluation of a compact, high-efficency neutron scatter camera," *Nuclear Instruments and Methods in Physics Research Section A: Accelerators, Spectrometers, Detectors and Associated Equipment*, vol. 883, pp. 115–135, 2018.

[28] C. Piemonte and A. Gola, "Overview on the main parameters and technology of modern silicon photomultipliers," *Nuclear Instruments and Methods in Physics Research Section A: Accelerators, Spectrometers, Detectors and Associated Equipment*, vol. 926, pp. 2–15, 2019. Silicon Photomultipliers: Technology, Characterisation and Applications.

[29] V. A. Li, T. M. Classen, S. A. Dazeley, M. J. Duvall, I. Jovanovic, A. N. Mabe, E. T. Reedy, and F. Sutanto, "A prototype for sandd: A highly-segmented pulse-shape-sensitive plastic scintillator detector incorporating silicon photomultiplier arrays," *Nuclear Instruments and Methods in Physics Research Section A: Accelerators, Spectrometers, Detectors and Associated Equipment*, vol. 942, p. 162334, 2019.

[30] F. Sutanto, T. Classen, S. Dazeley, M. Duvall, I. Jovanovic, V. Li, A. Mabe, E. Reedy, and T. Wu, "Sandd: A directional antineutrino detector with segmented 6li-doped pulse-shape-sensitive plastic scintillator," *Nuclear Instruments and Methods in Physics Research Section A: Accelerators, Spectrometers, Detectors and Associated Equipment*, vol. 1006, p. 165409, 2021.

[31] A. D. Francesco, R. Bugalho, L. Oliveira, L. Pacher, A. Rivetti, M. Rolo, J. Silva, R. Silva, and J. Varela, "TOFPET2: a high-performance ASIC for time and amplitude measurements of SiPM signals in time-of-flight applications," *Journal of Instrumentation*, vol. 11, p. C03042, Mar 2016.

[32] G. C. Rich, K. Kazkaz, H. P. Martinez, and T. Gushue, "Development of a lithium-glass based composite neutron detector for ^{3}He replacement," Tech. Rep. LLNL-TR-566675, Lawrence Livermore National Laboratory, 2012.

[33] M. Mayer, J. Natress, C. Trivelpiece, and I. Jovanovic, "Geometric optimizaton of a neutron detector based on a lithium glass-polymer composite," *Nuclear Instruments and Methods in Physics Research Section A: Accelerators, Spectrometers, Detectors and Associated Equipment*, vol. 784, pp. 168–171, 2015.

[34] J. Iwanowska, L. Swiderski, and M. Moszynski, "Liquid scintillators and composites in fast neutron detection," *Journal of Instrumentation*, vol. 7, p. C04004, 2012.

[35] D. V. Postovarova, A. V. Evsenin, A. Kuznetov, and O. Osetrov, "A method for measuring the energy spectrum of neutrons with energies of 1–15 MeV," *Instruments and Experimental Techniques*, vol. 57, pp. 28–32, 2014.

[36] N. Menaa, M. Villani, S. Croft, R. B. McElroy, S. A. Phillips, and J. B. Czirr, "Evaluation of lithium gadolinium borate capture-gated spectrometer neutron efficiencies," *IEEE Transactions on Nuclear Science*, vol. 56, pp. 911–914, 2009.

[37] S. Lam, J. Fiala, M. Hackett, and S. Motakef, "A high-performance CLYC(Ce)-PVT composite for neutron and gamma detection," *IEEE Transactions on Nuclear Science*, vol. 65, pp. 609–615, 2018.

[38] F. L. Ruta, S. Lam, J. Fiala, I. Khodyuk, and S. Motakef, "Monte Carlo simulation of a $Cs_2^6LiYCl_6$:Ce-based composite scintillator for neutron and gamma detection," *Nuclear Instruments and Methods in Physics Research Section A: Accelerators, Spectrometers, Detectors and Associated Equipment, in press.*

[39] A. Foster, A. Meddeb, M. Wonders, M. Flaska, M. Sharma, Z. Ounaies, and I. Jovanovic, "On the fabrication and characterization of heterogeneous composite neutron detectors with triple-pulse-shape-discrimination capability," *Nuclear Instruments and Methods in Physics Research Section A: Accelerators, Spectrometers, Detectors and Associated Equipment*, vol. 954, p. 161681, 2020.

[40] Eljen Technology, "Plastic Scintillator Casting Resin EJ-290." Datasheet, 2021.

[41] Scintacor, "Glass Scintillators." Datasheet, 2022.

[42] J. B. Czirr, D. B. Merrill, D. Buehler, T. K. McKnight, J. L. Carroll, T. Abbott, and E. Wilcox, "Capture-gated neutron spectrometry," *Nuclear Instruments and Methods in Physics Research Section A: Accelerators, Spectrometers, Detectors and Associated Equipment*, vol. 476, pp. 309–312, 2002.

[43] T. Shi, J. Nattress, M. Mayer, M.-W. Lin, and I. Jovanovic, "Neutron spectoscropy by thermalization light yield measurement in a composite heterogenous scintillator," *Nuclear Instruments and Methods in Physics Research Section A: Accelerators, Spectrometers, Detectors and Associated Equipment*, vol. 839, pp. 86–91, 2016.

[44] P. B. Rose, A. S. Erickson, M. Mayer, J. Nattress, and I. Jovanovic, "Uncovering special nuclear materials by low-energy nuclear reaction imaging," *Scientific Reports*, vol. 6, p. 24388, 2016.

[45] J. Nattress, K. Ogren, A. Foster, A. Meddeb, Z. Ounaies, and I. Jovanovic, "Discriminating uranium isotopes using the time-emission profiles of long-lived delayed neutrons," *Phys. Rev. Appl.*, vol. 10, p. 024049, 2018.

[46] K. Ogren, J. Nattress, and I. Jovanovic, "Discriminating uranium isotopes based on fission signatures induced by delayed neutrons," 2019.

[47] A. Foster, *Polyvinyl Toluene and Lithium Glass Composites for Neutron Detection*. PhD thesis, University Park, PA, 2019.

[48] S. Agostinelli, J. Allison, K. Amako, J. Apostolakis, H. Araujo, P. Arce, M. Asai, D. Axen, S. Banerjee, G. Barrand, F. Behner, *et al.*, "GEANT4—A simulation toolkit," *Nuclear Instruments and Methods in Physics Research Section A: Accelerators, Spectrometers, Detectors and Associated Equipment*, vol. 506, pp. 256–303, 2003.

[49] Z. S. Hartwig, "The ADAQ framework: An integrated toolkit for data acquisition and analysis with real and simulated radiation detectors," *Nuclear Instruments and Methods in Physics Research Section A: Accelerators, Spectrometers, Detectors and Associated Equipment*, vol. 815, pp. 42–49, 2016.

[50] M. J. I. Balmer, K. A. A. Gamage, and G. C. Taylor, "Comparative analysis of pulse shape discrimination methods in a ^{6}Li loaded plastic scintillator,"

Nuclear Instruments and Methods in Physics Research Section A: Accelerators, Spectrometers, Detectors and Associated Equipment, vol. 788, pp. 146–153, 2015.

[51] A. Simpson, S. Jones, M. Clapham, and S. McElhaney, "A review of neutron detection technology alternatives to helium-3 for safeguards applications," in *INMM 52nd Annual Meeting*, vol. 8, 2011.

[52] R. C. Byrd, "Directional fast-neutron detector," 1 1994.

[53] A. Galindo-Tellez, K. Keefe, E. Adamek, E. Brubaker, B. Crow, R. Dorrill, A. Druetzler, C. Felix, N. Kaneshige, J. Learned, J. Manfredi, K. Nishimura, B. P. Souza, D. Schoen, and M. Sweany, "Design and calibration of an optically segmented single volume scatter camera for neutron imaging," *Journal of Instrumentation*, vol. 16, p. P04013, apr 2021.

[54] L. Stevanato, D. Fabris, X. Hao, M. Lunardon, S. Moretto, G. Nebbia, S. Pesente, L. Sajo-Bohus, and G. Viesti, "Light output of ej228 scintillation neutron detectors," *Applied Radiation and Isotopes*, vol. 69, no. 2, pp. 369–372, 2011.

[55] N. Zaitseva, B. L. Rupert, I. Pawełczak, A. Glenn, H. P. Martinez, L. Carman, M. FAust, N. Cherepy, and S. Payne, "Plastic scintillators with efficient neutron/gamma pulse shape discrimination," *Nuclear Instruments and Methods in Physics Research Section A: Accelerators, Spectrometers, Detectors and Associated Equipment*, vol. 668, pp. 88–93, 2012.

[56] N. Zaitseva, A. Glenn, H. P. Martinez, L. Carman, I. Pawełczak, M. Faust, and S. Payne, "Pulse shape discrimination with lithium-containing organic scintillators," *Nuclear Instruments and Methods in Physics Research Section A: Accelerators, Spectrometers, Detectors and Associated Equipment*, vol. 729, pp. 747–754, 2013.

[57] A. N. Mabe *et al.*, "Transparent plastic scintillators for neutron detection based on lithium salicylate," *Nuclear Instruments and Methods.*, vol. A806, pp. 80–86, 2016.

[58] J. S. Carlson and P. L. Feng, "Melt-cast organic glasses as high-efficiency fast neutron scintillators," *Nucl.Instrum.Meth.*, vol. A832, pp. 152–157, 2016.

[59] W. M. Steinberger, M. L. Ruch, N. Giha, A. D. Fulvio, P. Marleau, S. D. Clarke, and S. A. Pozzi, "Imaging special nuclear material using a handheld dual particle imager," *Scientific Reports*, vol. 10, no. 1, 2020.

[60] V. Li, F. Sutanto, T. Classen, S. Dazeley, I. Jovanovic, and T. Wu, "Evaluation of a positron-emission-tomography-based SiPM readout for compact segmented neutron imagers," *Nuclear Instruments and Methods in Physics Research Section A: Accelerators, Spectrometers, Detectors and Associated Equipment*, vol. 1046, p. 167624, 2023.

[61] M. Li and S. Abbaszadeh, "Depth-of-interaction study of a dual-readout detector based on TOFPET2 application-specific integrated circuit," *Physics in Medicine and Biology*, vol. 64, 2019.

[62] E. Lamprou, F. Sanchez, J. M. Benlloch, and A. J. Gonzalez, "In-depth evaluation of TOF-PET detectors based on crystal arrays and the TOFPET2 ASIC," *Nuclear Instruments and Methods in Physics Research Section A: Accelerators, Spectrometers, Detectors and Associated Equipment*, vol. 977, p. 164295, 2020.

[63] V. Nadig, D. Schug, B. Weissler, and V. Schulz, "Evaluation of the PETsys TOFPET2 ASIC in multi-channel coincidence experiments.," *EJNMMI Physics*, vol. 8, no. 1, 2021.

[64] V. Nadig, M. Yusopova, H. Radermacher, D. Schug, B. Weissler, V. Schulz, and S. Gundacker, "A Comprehensive Study on the Timing Limits of the TOFPET2 ASIC and on Approaches for Improvements," *IEEE Transactions on Radiation and Plasma Medical Sciences*, vol. 6, no. 8, pp. 893–903, 2022.

[65] M. Wang, Y. Wang, and L. Wang, "Evaluation of high-resolution and depth-encoding PET detector modules based on single-ended readout with TOFPET2 ASIC," *Radiat Detect Technol Methods*, vol. 5, pp. 451–458, 2021.

[66] T. Binder, H. Kang, M. Nitta, F. Schneider, T. Yamaya, K. Parodi, F. Wiest, and P. Thirolf, "Performance evaluation of a staggered three-layer DOI PET detector using a 1-mm LYSO pitch with PETsys TOFPET2 ASIC: comparison of HAMAMATSU and KETEK SiPMs," *Physics in Medicine and Biology*, vol. 66, 2021.

[67] M. Sweany, L. D. Claus, P. L. Feng, M. D. Gerling, J. S. Mincey, P. E. Maggi, P. Marleau, L. Nguyen, and H. Tran, "Pixelated Silicon Photomultipler readout and organic scintillator detector assemblies," vol. SAND2021-3147C, Mar 2021.

[68] R. Bugalho, A. Di Francesco, L. Ferramacho, C. Leong, T. Niknejad, L. Oliveira, L. Pacher, M. Rolo, A. Rivetti, and M. e. a. Silveira, "Experimental results with TOFPET2 ASIC for time-of-flight applications," *Nuclear Instruments and Methods in Physics Research Section A: Accelerators, Spectrometers, Detectors and Associated Equipment*, vol. 912, pp. 195–198, 2018.

[69] S. Seifert, H. T. van Dam, R. Vinke, P. Dendooven, H. Lohner, F. J. Beekman, and D. R. Schaart, "A Comprehensive Model to Predict the Timing Resolution of SiPM-Based Scintillation Detectors: Theory and Experimental Validation," *IEEE Transactions on Nuclear Science*, vol. 59, no. 1, pp. 190–204, 2012.

[70] PETsys Electronics, "PETsys TOF ASIC evaluation kit." Flyer, 2019.

[71] L. Ferramacho and S. Tavernier and V. A. Li and T. C. Wu, "Private conversations with manufacturer." Private communcation, 2020.

[72] L. Gruber, S. Brunner, J. Marton, and K. Suzuki, "Over saturation behavior of SiPMs at high photon exposure," *Nuclear Instruments and Methods in Physics Research Section A: Accelerators, Spectrometers, Detectors and Associated Equipment*, vol. 737, pp. 11–18, 2014.

[73] L. H. C. Braga, L. Gasparini, L. Grant, R. K. Henderson, N. Massari, M. Perenzoni, D. Stoppa, and R. Walker, "A Fully Digital 8×16 SiPM Array for PET Applications With Per-Pixel TDCs and Real-Time Energy Output," *IEEE Journal of Solid-State Circuits*, vol. 49, no. 1, pp. 301–314, 2014.

[74] W. Hansen and D. Richter, "Determination of light output function and angle dependent correction for a stilbene crystal scintillation neutron spectrometer," *Nuclear Instruments and Methods in Physics Research Section A: Accelerators, Spectrometers, Detectors and Associated Equipment*, vol. 476, no. 1, pp. 195–199, 2002. Int. Workshop on Neutron Field Spectrometry in Science, Technology and Radiation Protection.

[75] M. L. Ruch, M. Flaska, and S. A. Pozzi, "Pulse shape discrimination performance of stilbene coupled to low-noise silicon photomultipliers," *Nuclear Instruments and Methods in Physics Research Section A: Accelerators, Spectrometers, Detectors and Associated Equipment*, vol. 793, pp. 1–5, 2015.

[76] J. W. Bae, T. C. Wu, and I. Jovanovic, "Reconstruction of fast neutron direction in segmented organic detectors using deep learning," *Nuclear Instruments and Methods in Physics Research Section A: Accelerators, Spectrometers, Detectors and Associated Equipment*, p. 168024, 2023.

[77] Liquid O Consortium, "Neutrino physics with an opaque detector," *Communications Physics*, vol. 4, no. 1, p. 273, 2021.

[78] A. S. Wilhelm, G. Wendel, B. Collins, D. Cowen, and I. Jovanovic, "Evaluation of light collection from highly scattering media using wavelength-shifting fibers," *Nuclear Instruments and Methods in Physics Research Section A: Accelerators, Spectrometers, Detectors and Associated Equipment*, vol. 1049, p. 168085, 2023.